



Technische Universität München
Institut für Technische Chemie
Prof. Dr. Johannes A. Lercher



UNIVERSITÉ
LAVAL

Université Laval
Département de Génie Chimique
Prof. Serge Kaliaguine Ph.D.

SBA-16 MATERIALS

SYNTHESIS, DIFFUSION AND SORPTION PROPERTIES

Author: Oliver Christian Gobin
Adviser: Prof. Serge Kaliaguine Ph.D.
Laval University, Ste-Foy, Quebec, Canada, January 2006

Contents

Acknowledgments	iii
Symbols and abbreviations	iv
1. Introduction and motivation	1
2. Fundamentals of bi-porous materials	2
2.1. Porous materials	2
2.2. Synthesis of mesoporous siliceous materials	3
2.2.1. Silica polymerization	3
2.2.2. Concept of templating	4
2.3. Overview of micro and mesoporous materials	6
2.3.1. Materials with hexagonal symmetry	7
2.3.2. Materials with cubic symmetry	8
2.4. Evolution of bi-porous materials	10
3. Methods and calculations	14
3.1. Physisorption	14
3.1.1. Theoretical isotherms	15
3.1.2. The BET-surface analysis	16
3.1.3. Micropore analysis	17
3.1.4. Pore size distributions	18
3.1.5. Measurements	20
3.2. X-ray diffraction (XRD)	20
3.3. Small angle X-ray scattering (SAXS)	21
3.4. Transmission electron microscopy (TEM)	21
3.5. Scanning electron microscopy (SEM)	22
3.6. Zero length column (ZLC) chromatography	23
3.6.1. Introduction	23
3.6.2. Experimental set-up	24
3.6.3. Differential ZLC Model	25
3.6.4. Measurements	26
3.7. Adsorption of hydrocarbons	27
3.7.1. Experimental set-up	27
3.7.2. Data analysis and calculations	28

4. Synthesis and characterization	29
4.1. Synthesis of SBA-16 materials	29
4.2. Results and Discussions	30
4.2.1. Morphology	30
4.2.2. Crystallographic structure	31
4.2.3. Mesoporous properties	34
4.2.4. Microporous and intrawall properties	37
4.3. Conclusions	41
5. Diffusional properties	42
5.1. Theory	42
5.2. Measurements and calculations	42
5.3. Results and Discussions	43
5.4. Conclusions	50
6. Adsorption of hydrocarbons	51
6.1. Results and Discussion	51
7. Conclusions and perspectives	56
A. Derivation of model equations	57
A.1. Differential ZLC-Model	57
B. Source codes	60
B.1. Matlab source codes	60
B.2. SigmaPlot macros	63
References	64

Acknowledgments

First, I would like to thank my thesis adviser, Professor Serge Kaliaguine, for giving me the opportunity to work in his group at Laval University and to explore the field of materials chemistry and chemical engineering science. I am deeply grateful for his valuable advice, motivation and competent guidance during my stay in Canada. I really appreciated the freedom I was given.

I wish especially to thank my thesis co-adviser Professor Freddy Kleitz, who introduced and guided me during the synthesis and characterization of SBA-16 materials. I like to thank him for the fruitful and stimulating discussions and for all the advice he gave me.

I wish also to thank Professor Mladen Eic in the Department of Chemical Engineering of University of New Brunswick in Fredericton, for the chance to work in his group during the second part of my stay in Canada.

I am sincerely grateful to Professor Johannes A. Lercher, who established a connection with Professor Serge Kaliaguine and gave me the possibility to write my seminar thesis.

I am very grateful for the help from all my colleagues at Laval University and University of New Brunswick. I also like to give special thanks to Dr. Qinglin Huang for introducing me to the ZLC technique and for all his advice and help during the analysis of the diffusion and sorption experiments.

Special thanks are due to Dr. Hendrik Dathe and Peter Haider, who supervised me during my preparatory work at Professor Lercher's group prior to my stay in Canada. Both Hendrik and Peter introduced me in experimental work and gave me new ideas, as for instance the use of statistical methods in formulating and solving problems in chemistry.

I gratefully thank Professor Freddy Kleitz and Professor Dongyuan Zhao for performing the XRD, SAXS and TEM investigations on the SBA-16 series and Anastasia Schneider for the proof-reading of the manuscript.

Finally, I wish to thank my family for their invaluable personal and financial support, their understanding and patience.

This work is dedicated to my family, my mother, my father and my brother.

Symbols and abbreviations

Latin symbols

A, B	(-)	dimensionless parameters (ZLC value)
a, b, c	(m)	unit cell parameters
c	(mol m ⁻³)	concentration of the sorbates in the fluid phase
d_{hkl}	(m)	spacing between the (hkl) planes
D	(m)	diameter
D	(m s ⁻¹)	intracrystalline diffusivity
E	(J)	energy
F	(m ³ s ⁻¹)	flow rate
h_w	(m)	wall thickness
h	(-)	Miller index
H	(J)	enthalpy
k	(-)	Miller index, control variable
K	(-)	adsorption equilibrium constant
K_H	(-)	Henry constant
l	(-)	Miller index
n	(-)	BET parameter, degree of order, control variable
p	(Pa)	pressure
q	(mol m ⁻³)	concentration of the adsorbed phase
q	(m ⁻¹)	q -value of a scattering experiment
Q_{hkl}	(-)	crystallographic parameter depending on the space group
r		radial coordinate
r, R	(m)	radius
R	(m ² kg s ⁻² mol ⁻¹ K ⁻¹)	molar universal gas constant
S	(m ² kg ⁻¹)	specific surface area
t	(s)	time variable or coordinate
t	(m)	statistical thickness of the adsorbed nitrogen layer
T	(K)	temperature
L	(-)	dimensionless parameter (ZLC value)
v	(m s ⁻¹)	velocity of the fluid
V	(m ³ kg ⁻¹)	specific volume
x	(-)	relative pressure ($x = p/p_0$)
x, y, z		coordinates

SYMBOLS AND ABBREVIATIONS

Greek symbols

β	(-)	positive root (ZLC value)
ϵ	(-)	porosity
λ	(m)	wavelength
λ		constant (ZLC value)
μ	(-)	number of cavities per unit cell
π	(-)	number Pi
γ	()	surface tension
γ	(-)	dimensionless parameter (ZLC value)
ρ	(kg m ⁻³)	density
θ	(degree)	angle
θ	(-)	normalized isotherm

Indices

0	reference or initial value
1,2	first and second microporosity
ads	adsorption
c	core
des	desorption
eff	effective
exp	experimental value
ext	external property
f	fluid-phase
hkl	value as a function of the Miller indices
i, j, k, m, n	control variables
max	maximum
me	mesoporous property
mi	microporous property
min	minimum
s	solid-phase
t	total

SYMBOLS AND ABBREVIATIONS

Abbreviations

BET	Brunauer-Emmett-Teller plot
BJH	Barret-Joyner-Halenda method
CMT	critical micelle temperature
CMC	critical micelle concentration
CMK	ordered mesoporous carbon number
DSBM	Dual Site-Bond Model
EDX	energy dispersive X-ray microanalysis
FCC	fluid catalytic cracking
FID	flame ionization detector
HR-TEM	high resolution transmission electron microscopy
I	inorganic component (silica source)
IUPAC	International Union of Pure and Applied Chemistry
KIT- x	Korean Institute of Technology number x
KJS	Kruk-Jaroniec-Sakamoto method
MCM- x	Mobil Composition of Matter number x
MD	molecular dynamics simulation
MSC	model of spherical cavities
N	non-ionic surfactant
NLDFT	non local density function theory
NMR	nuclear magnetic resonance
PAA	poly(acrylic acid)
PE	polyethylene
PEO	poly(ethylene oxide)
PEP	positron emission profiling
PFG	pulsed field gradient
PI	polyimide
Pluronic P123	(ethylene oxide) ₂₀ -(propylene oxide) ₇₀ -(ethylene oxide) ₂₀
Pluronic F127	(ethylene oxide) ₁₀₆ -(propylene oxide) ₇₀ -(ethylene oxide) ₁₀₆
PPO	poly(propylene oxide)
PS	polystyrol
PSD	pore size distribution
QENS	quasi-elastic neutron scattering
S	surfactant
SAXS	small angle X-ray scattering
SBA- x	Santa-Barbara number x
SEM	scanning electron microscopy
STP	standard temperature and pressure conditions
TEM	transmission electron microscopy
TEOM	tapered element oscillating microbalance
TEOS	tetraethyl orthosilicate
TAP	temporal analysis of products
TST	transition state theory
XRD	X-ray diffraction
ZLC	zero length column chromatography

1. Introduction and motivation

The focus of this seminar thesis is the synthesis and characterization of a recently developed kind of porous silicate material. The development of new kinds of highly specialized materials and their characterization is fundamental for many fields of industrial application and engineering science. The proper characterization involves their microscopic as well as their macroscopic properties. Often only one of these properties is well investigated, but only the combination of both properties leads to a holistic analysis.

In this thesis, a series of SBA-16 materials was synthesized and characterized by microscopic and macroscopic techniques, as for instance the diffusion of hydrocarbons through SBA-16 particles. It is build-up on several prior studies on a series of SBA-15 materials investigated by Huang et al. The comparison and discussion of differences will be a major issue.

The structure of this thesis is in brief:

- Chapter 2 gives an overview on relevant aspects on porous materials and on their evolution during the synthesis. The time and temperature dependent self-assembly of these materials is fundamental to this thesis, because precisely these parameters were used to obtain SBA-16 materials with strongly varying structural properties.
- The third chapter gathers the relevant characterization techniques and discusses their applicability and their mathematical or numerical implementation.
- Chapter 4 gives a brief summary of the synthesis of SBA-16 materials. The main aspect of this chapter is the proper investigation of microporous properties of the SBA-16 series. This involves the exact determination of pore structure and crystallographic characteristics.
- Chapter 5 combines the prior results with a macroscopic method to measure intracrystalline diffusivities, the so called zero length column (ZLC) method. It is the first time, that diffusivities in such a structure as SBA-16 were investigated.
- Chapter 6 involves the adsorption of hydrocarbons on the SBA-16 series, which are directly related to the diffusion studies. Unfortunately this chapter has become rather short, due to a lack of experimental data.

2. Fundamentals of bi-porous materials

2.1. Porous materials

Porous materials have attracted the interest of scientists and industry due to various applications for instance in molecular separation, heterogeneous catalysis, adsorption technology or opto-electronics as well as new challenges in the fundamental material research.

In general the surface area of a porous material is higher than the surface of an analogous non-porous material. Thereby the internal surface area is usually much higher than the one contributed by the external surface. Due to the fact that heterogeneous catalyzed chemical reactions basically occur on surfaces or at phase boundaries, a higher surface area would, theoretically, directly yield to an improved reactivity. In reality different kind of limitations can occur and have to be taken into consideration. Apart of the surface area other important characteristics of porous solids are the crystallinity or regularity if present, the distribution of pore sizes and the chemistry of the walls. In an ideal porous material these attributes should be tailored exactly to the needs of the application. To be commercially interesting, such a material should be inexpensive and highly stable for regeneration. Materials based on silicate show up such kind of flexibility and have hence found wide fields of industrial applications.

In this chapter I will give a brief introduction to porous materials with a focus on ordered silicate materials with a micro and mesoporosity. According to the IUPAC definition [1] micropores are pores with diameter under 2 nm, mesopores with diameter between 2 and 50 nm and macropores have diameters greater than 50 nm. Corresponding to this definition, materials can be 'labeled' as solids with a certain porosity. Examples of microporous materials are Zeolites. A well-known mesoporous material is MCM-41 (Mobil Composition of Matter No 41) with highly ordered pores. In this work bi-porous materials should be defined as materials containing both micro and mesopores. The MCM-41 bi-porous counterpart is SBA-15 (Santa Barbara No 15). Macroporous materials are for example porous glasses or gels.

Zeolites are highly crystalline aluminosilicates with an extremely narrow distribution of micropores. Due to the well defined structure and large surface area, zeolites are widely deployed in very specific applications for example in the oil industry as catalyst for cracking, alkylation or shape selective catalysis, as molecular sieves or as adsorbates. The most important limitation for application are their small pore sizes up to only 1.2 nm so far. Molecules that just suit the pore size are inhibited and do not show high diffusivities, larger molecules with critical diameters even larger than the pore, will not be able to enter the pore. Hence for catalysis of large molecules or to improve the diffusivities

larger pores are required. A new kind of material very similar to SBA-15, but having walls made of ZSM-5, seems to combine the crystallographic advantages of Zeolites and the pore structure of MCM-41 or SBA-15. Also this material has a superior thermal, hydrothermal and mechanical stability compared to SBA-15. It is made by replication using CMK-3 materials [2].

Another important type of porous materials, but not on the basis of silicate, are porous carbons [3, 4, 5]. Ordered porous carbons can be made by nanocasting using mesoporous silicate as template [6, 7, 8]. One gets a negative replication of the mesoporous template. Porous carbons exhibit interesting properties such as the hydrophobic nature of their surface, chemical inertness, good mechanical and thermal stability as well having advantages to form membranes, tubes or fibers [9]. Other types of porous materials are for example porous coordination solids or porous heteropolyanion salts.

The main focus of this work will be porous materials based on silicate containing both micro- and mesopores or only mesopores. Zeolites and other types of porous materials will not be a major issue.

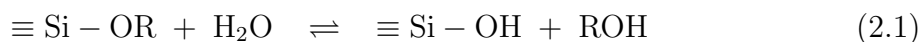
2.2. Synthesis of mesoporous siliceous materials

2.2.1. Silica polymerization

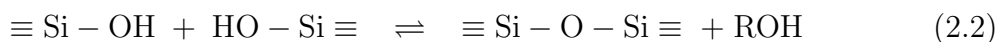
The classical way of silica polymerization, the so called sol-gel process, is carried out in an aqueous solution as Iler [10] investigated in 1979. This process is rather uncontrolled leading to non or poorly ordered structures with broad pore size and molecular weight distributions. These porous silica are known as sol-gel materials like aerogels or xerogels. The pathways leading to ordered porous materials are very similar to the sol-gel process and will be described in the next section.

As stated before, the polymerization is carried out in an aqueous solution by adding a catalyst and a source of silica. The silica source is an important factor for the reaction conditions. Common molecular sources are alkoxysilanes like tetramethyl- and tetraethylorthosilicate or sodium silicate. Non-molecular silica sources are for example already polymerized sol-gel materials which are leading to non-homogeneous solutions.

The first step of polymerization is the formation of silanol groups by hydrolysis of the alkoxide precursors, the gel, in aqueous solution:



The actual polymerization occurs through water (oxolations) or alcohol (alcoxolations) producing condensations:



This polycondensation reaction leads to more or less cross linked polysilicates which are precipitating during the reaction. This dispersion is called the sol. All the reactions are strongly pH dependent. They can be catalyzed by acid or base catalyst under formation of cationic (under acidic conditions) or anionic silicate species. Acid catalysts produces weakly-crosslinked gels which easily compact under drying conditions, yielding low-porosity microporous xerogel structures. Conditions of neutral to basic pH result in relatively micro- and mesoporous xerogels after drying.

Under some conditions, base-catalyzed and two-step acid-base catalyzed gels (initial polymerization under acidic conditions and further gelation under basic conditions) exhibit hierarchical structure and complex network topology [11, 12].

2.2.2. Concept of templating

The main concept to obtain well defined and structured polysilicates is to use a surfactant templated polymerization instead of an uncontrolled reaction. In general the lyotropic (i.e. amphiphilic) molecules of the surfactant form a liquid crystal by aggregation in aqueous solution [13, 14]. Of course the proper formation of the liquid crystal matrix is strongly dependent on the conditions in the solution. The structure of the liquid crystal is the so called mesostructure. Important parameters for the mesophase formation are for instance the temperature (CMT), the concentration (CMC) or the pH-value of the solution. Depending on these conditions, the structure of the mesophase can be for example ordered in spherical, cylindrical, lamellar or cubic phase or disordered. Two distinct families of phases exist. One type is based on periodic continuous minimal boundary surfaces of the phase components, the other type is micellar being based on packing of discrete micellar aggregates. Especially for the cubic phase the cubic micellar 'I' and the bicontinuous cubic phases can be well-defined. Later in this chapter some examples of materials synthesized in a micellar or bicontinuous mesophase will be given. A detailed study of the polymorphism of lipid water systems was done by Seddon and Templer [15]. In Figure 2.1 examples of lyotropic mesophases in such liquid crystal systems are visualized.

To act as a structure directing agent, the mesophase has to interact in some way with the silica precursors. There have been many different attempts to develop pathways to influence the interactions between mesophase and polycondensation reaction of the silica source. These are in particular alkaline routes (S^+I^-), acidic routes ($S^+X^-I^+$) or non-ionic (S^0I^0) and neutral (N^0I^0) routes. Where S is standing for the surfactant molecules, I for the silica source, X^- for halides and N for a non ionic surfactant. The difference of the routes is mostly the kind of driving force, which can be ionic-ionic, ionic-metal in the case of the ionic routes or hydrogen-bonding interactions in the case of non-ionic routes.

The ionic routes were developed in the early 1990s by Beck et al. [13, 14] and have been intensively studied so far. They lead to monoporous¹ materials like the MCM family. These ionic routes will not be of major interest for this work. For completeness they will just be briefly described. In contrast newer non ionic routes yield to bi-porous

¹monoporous: only mesopores

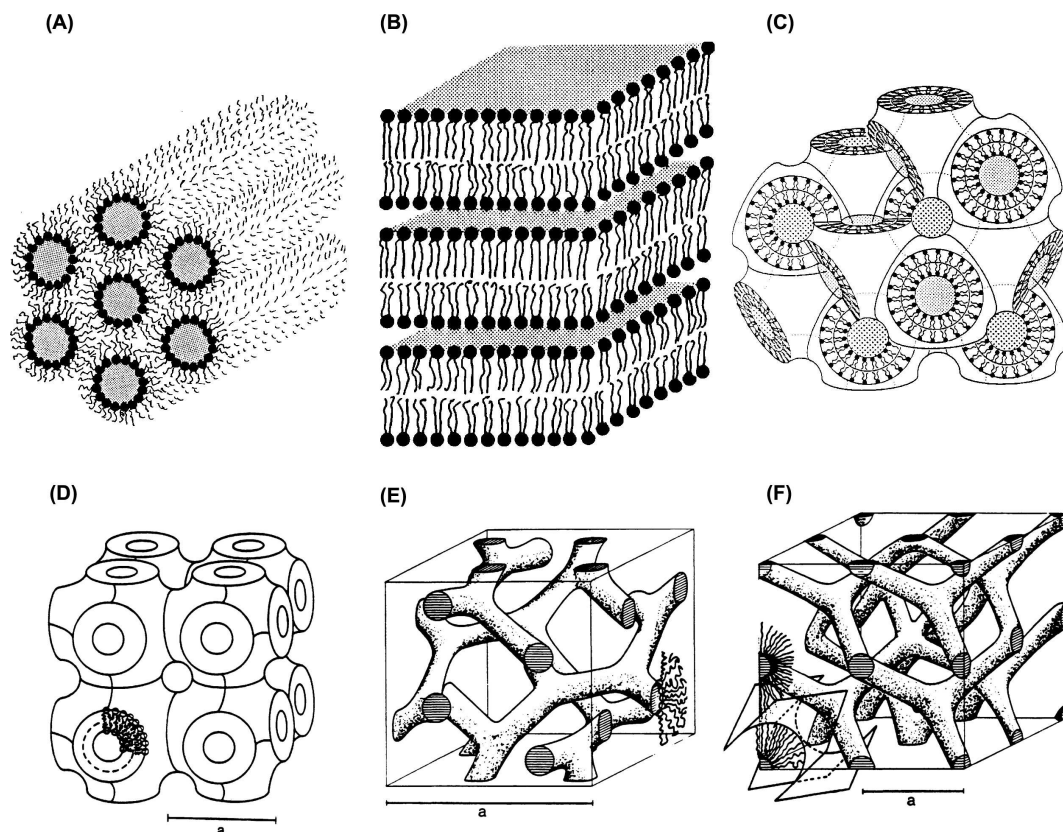


Figure 2.1.: Examples of lyotropic structures of surfactant/water systems. (A) inverse hexagonal H_{II} phase; (B) L_{α} fluid lamellar phase; (C) inverse bicontinuous cubic phase $Pn\bar{3}m$; (D) Schwarz's P-surface ($Pm\bar{3}m$); (E) inverse bicontinuous cubic phase $Ia\bar{3}d$ in 'rod-like' representation; (F) 'rod-like' representation of subfigure (C), from Seddon and Templer [15].

materials with generally larger primary mesopores and thicker walls than the counterparts templated with ionic surfactants.

The size and the range of the interactions in the solution with the silicate molecules can be furthermore varied by changing the ionic strength of the solution using inorganic salts to form halides or metal cations in alkaline or acidic medium (S^+I^- , $S^+X^-I^+$). For the non-ionic route, cosurfactants like alcohols can be added to vary the molecule interaction in solution.

Ionic routes

The first attempts to synthesize ordered mesoporous silica were done under ionic conditions. Under these conditions the inorganic silicates I and also the surfactant molecules S are charged depending on the pH-value of the solution.

The well known mesoporous candidates from the MCM family are typically synthesized under alkaline conditions. Under these condition the silicates are deprotonated and form anions I^- and the surfactant molecules form cations S^+ respectively. Three different mesophases could be observed for this system leading to three structures, the hexagonal MCM-41, the cubic MCM-48 and the lamellar MCM-50. The exact reaction conditions can be found in many publications [16, 17].

The first attempts to synthesize templated mesoporous silica under acidic conditions were carried out by Huo et al. [18, 19, 20]. At these conditions the cationic surfactant molecules are surrounded by negative halides. A triple layer of surfactant, halides and the cationic silicate species ($S^+X^-I^+$) is the considered mechanism for the mesophase formation. Mesoporous materials synthesized using this route are for instance the SBA-3 materials.

Non-ionic routes

More important for this work are the non-ionic routes templated with amphiphilic triblock copolymers. These routes are relatively new and have shown a high flexibility in tailoring the synthesis conditions and the mesostructure of the liquid crystal template. Especially the easy variation of hydrophobic/hydrophilic copolymer blocks and thus their volume fraction simply by using different chain length or cosurfactants provides a high degree of control. Commonly used block components are hydrophobic polymers like PPO, PS, PI or PE and hydrophilic polymers like PEO and PAA.

Relevant for this thesis is the ternary water, butanol, triblock copolymer (Pluronic P123 or F127) system at low acid concentrations. Kleitz et al. [23] recently established several diagrams of the synthesis product phases, which clearly visualize the effects of concentration of several components. In Figure 2.2 two product phase diagrams for these systems are shown. Figure 1A and 1B are reflecting the phase domains of the mesophase leading to SBA-15 (2-D hex domain), SBA-16 ($Im\bar{3}m$ domain), KIT-5 ($Fm\bar{3}m$ domain) and KIT-6 ($Ia\bar{3}d$ domain) or mixed and disordered materials. Figure 1C shows the influence of the cosurfactant/surfactant ratio leading to KIT-5, SBA-16 or SBA-15 materials if the mass ratio of BuOH:F127 is less than 2, 2 and higher 3 respectively. A detailed discussion of these routes at low acid concentration was published recently by Kleitz et al. [22, 24].

2.3. Overview of micro and mesoporous materials

The main purpose of this section is to give an overview of highly ordered porous materials with both meso and micropores relevant for this work. Their crystallographic and structure properties will be the major interest, focusing on important aspects for the later diffusion studies on these materials.

The diffusion and sorption of hydrocarbons has been carried out on two major types of materials. Materials with a 2-dimensional hexagonal were examined recently by

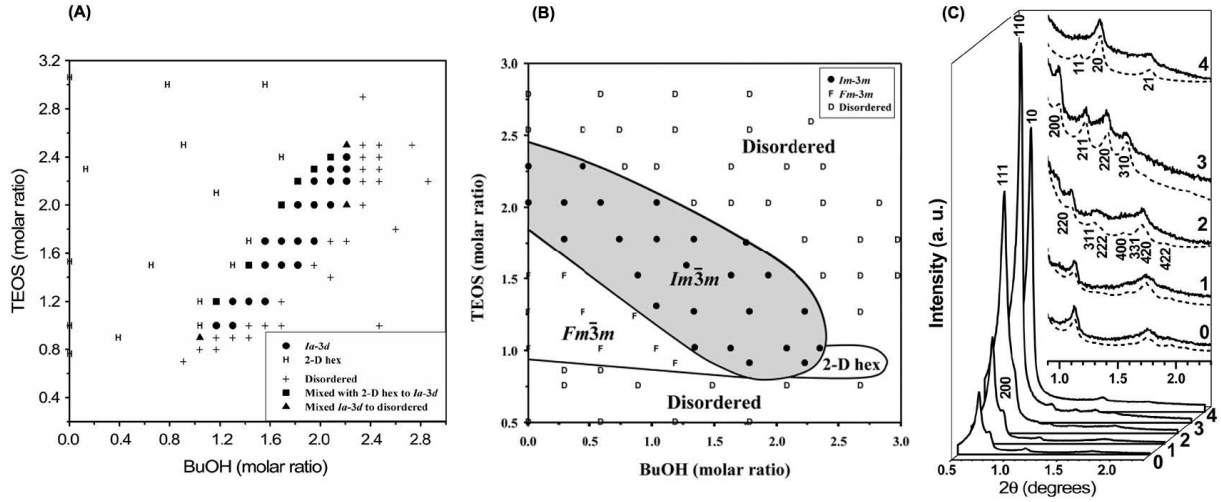


Figure 2.2.: (A) Phase domains of the ternary water, butanol, Pluronic P123 system with a molar ratio of 0.017 P123: x TEOS: y BuOH:1.83 HCl: 195 H₂O, from Kim et al. [21]; (B) Phase domains of the ternary water, butanol, Pluronic F127 system with a molar ratio of 0.0035 F127: x TEOS: y BuOH:0.91 HCl:117 H₂O, from Kleitz et al. [22]; (C) Experimental (solid line) and simulated (dashed line) XRD powder patterns of material synthesized using the ternary water, butanol, Pluronic F127 system with a mass ratio of BuOH:F127 = 0,1,2,3 and 4, from Kleitz et al. [23].

Hoang et al. [25] and materials with a 3-dimensinal cubic symmetry were investigated in this thesis.

2.3.1. Materials with hexagonal symmetry

MCM-41

In 1992 researchers from the Mobil Oil Company were the first to develop a synthesis route using *Liquid Crystal Templating* leading to a new family of mesoporous molecular sieves [13, 14]. For all these materials the mesophase is created using so called gemini surfactants (i.e. ternary ammonium compounds) under alkaline conditions. The MCM-41 materials are one species of these materials which have been the most investigated. They are mesoporous materials of cylindrical rod-like pores with diameters from 1.5 nm up to about 8 nm ordered in hexagonal arrays. The long range space group is $P6mm$. The pore walls are amorphous and relatively thin. The wall thickness is usually between 0.6 and 1.2 nm [26]. Due to the long rod-like pores this material is ideally homogeneous and isotropic only on a mesoscopic scale in one or two dimensions.

Typical pore size distributions are very narrow, an indication for a well ordered structure. The porosity only consists of mesopores without intrawall micropores. This leads to a one-dimensional diffusion through the pores.

MCM-41 materials have found various application in catalysis [27, 28, 29] and various techniques for characterization have been developed [3, 26, 30, 31, 32, 33, 34, 35, 36, 37, 38, 39]. They have a very high BET surface area up to 1000-1200 m²/g. The morphology, pore sizes and BET surface areas are highly adjustable during synthesis. Also the chemistry of the walls can be easily changed by incorporation of heteroatoms or grafting techniques [40, 41, 42, 43]. The most important limitation for example as FCC catalyst is the low hydrothermal stability of these materials [44, 45], caused by the rather thin and amorphous pore walls.

SBA-15

Very similar to MCM-41 materials are SBA-15 materials prepared under acidic conditions with the triblock copolymer Pluronic P123 (EO₂₀PO₇₀EO₂₀) surfactant as template [46, 47] (see Figure 2.2). The mesopores are ordered in hexagonal arrays providing the same long range space group as for MCM-41 materials (*P6mm*). However, due to the properties of the Pluronic type surfactant [48] SBA-15 materials show up important differences in porosity and adsorption properties compared to MCM-41 materials. In a regular synthesis, SBA-15 materials have much thicker but still amorphous walls and primary mesopore diameters between 5 nm to 15 nm. The BET surface area of SBA-15 is generally lower than the one of MCM-41. Due to thicker pore walls, they are hydrothermal more stable [43, 49]. Also due to the Pluronic surfactant type, SBA-15 materials generally have a second intrawall porosity consisting of micropores or smaller mesopores. These unordered pores interconnect the primary mesopore channels. It is possible to tailor the micro/mesopore ratio to the needs of the application, still conserving the rather thick pore walls. The intrawall microporosity is caused by the penetration of the hydrophobic PO groups of the blockcopolymer chain into the silica matrix. The wall thickness is caused by the length of these polymer chains.

2.3.2. Materials with cubic symmetry

SBA-16 and KIT-5

SBA-16 is a porous silica with large (5-15 nm) cage-like mesopores arranged in a three dimensional cubic body-centered *Im* $\bar{3}$ *m* symmetry [46, 50]. Like SBA-15 it is synthesized under acidic conditions using a non ionic Pluronic surfactant (Figure 2.2) and is therefore providing an intrawall complementary porosity [25]. The mesophase can be created using mixtures of Pluronic P123 and Pluronic F127 (EO₁₀₆PO₇₀EO₁₀₆) or in a ternary water, butanol and Pluronic F127 system. Caused by the longer PO chains in Pluronic F127 compared to Pluronic P123 SBA-16 generally has thicker pore walls than SBA-15.

The structure of SBA-16 can be described by a triply periodic minimal surface of I-WP (body centered, wrapped package) [50] as represented in Figure 2.3. The mesophase might also be a triply periodic minimal surface. As suggested by electron crystallography studies [50], each mesopore is connected to eight neighboring mesopores for SBA-16. Thereby

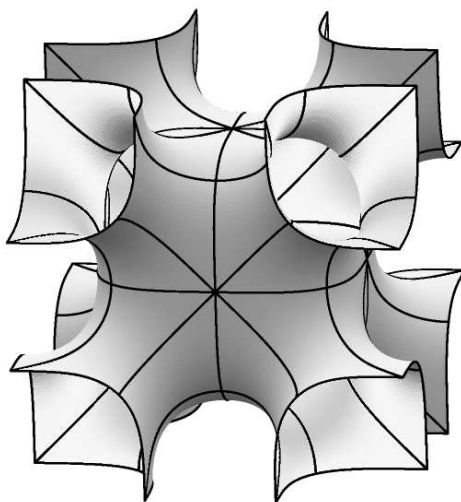


Figure 2.3.: Schoen's I-WP triply periodic minimal surface as a representation of the structure of SBA-16 materials and the corresponding mesophase, from Brakke [51].

the pore entrance size from one mesopore to another is usually significantly smaller than the primary mesopore size, making this size the limiting factor for applications involving intraparticle mass transfer. The desorption out of this kind of structure is dominated by so called pore blocking and networking effects [52, 53]. The primary mesopore size can relatively easy be obtained by diffraction or physisorption measurements in combination with an adapted geometric model like the model of spherical cavities or the triply periodic I-WP surface [52, 53]. In contrast, the pore entrance size is more difficult to obtain. Analyzing the PSD of the desorption physisorption isotherm a first guess of a maximal diameter is possible. If the desorption occurs spinodal at a pressure of about $0.48 - 0.50 p/p_0$ the pore entrance diameters are less than 4 nm. Larger sizes will cause a shift of the desorption isotherm towards higher pressures [54]. Pore entrance sizes greater than 4 nm can thus relatively straightforward be characterized by physisorption measurements. Using probe molecules of large kinetic diameters and analyzing their sorption properties it is also possible to characterize entrance sizes below 4 nm.

KIT-5 is also a porous silica with very similar properties than SBA-16. The mesopores are ordered in a cubic face-centered $Fm\bar{3}m$ symmetry. Like SBA-16 KIT-5 can be synthesized in a ternary water, butanol and Pluronic F127 surfactant system (Figure 2.2).

In contrast to the triply periodic bicontinuous minimal surface of the SBA-16 mesophase, for KIT-5 it is possible to have a cubic micellar mesophase. In this case each mesopore would only be statistically connected to each other, but arranged in a face-centered symmetry. The further structural properties, including the pore entrances to the primary mesopores, are very similar to SBA-16.

MCM-48 and KIT-6

MCM-48 and KIT-6 are both materials with a 3-dimensional $Ia\bar{3}d$ structure. The best representation of the structure is a gyroid minimal surface [55]. MCM-48 is synthesized in a similar way to MCM-41 under alkaline conditions with genimi surfactants. The pore wall thickness of MCM-48 is about 0.8 to 1.0 nm [55] just like for MCM-41 materials. The pore sizes are also in the same range as for MCM-41 materials. KIT-6 can be synthesized using as mesophase the ternary system shown in Figure 2.2A. Pore wall thickness and pore dimensions are in the same range as for SBA-15 materials.

The gyroid structure, which can be interpreted as two interwoven cylindrical channels, leads to adsorption properties which are similar to the one of the 2-dimensional hexagonal materials. The desorption is not kinetically limited and near equilibrium. Pore blocking effects are not occurring. These materials seem to combine the advantages of the 2-dimensional hexagonal with the one of a 3-dimensional structure. In this thesis the properties of these materials will not be further investigated, only for completeness and to promote further studies a short overview was given.

2.4. Evolution of bi-porous materials

In this section, especially the time and temperature dependency of mesophase and silica condensation and hence of the calcinated materials will be discussed. A good understanding of this behavior is important for the later work, where precisely these synthesis parameters were varied. Also they have been in the last few years some other interesting studies predominantly focusing on these synthesis parameters [25, 54].

As it will be shown later in the synthesis section, generally the synthesis of these materials is divided in a reaction period, where mostly the polymerization takes place and an aging (or hydrothermal treatment) period, where the molecules crystallize in part and try to reach a thermodynamic stable minimum. The reaction period is generally well stirred, whereas the aging period usually takes place under static conditions. The synthesis conditions during the reaction period are often kept constant. In this thesis the temperature and the time of the aging period were varied. Other parameters as for instance the pH-value of the solution or cosurfactants are of cause influencing all the steps involved during the formation of the materials, but for this study only the evolution period during the aging step is of importance and will be discussed in this section. Also only relevant surfactants, i.e. Pluronic block-copolymers are being considered. Detailed studies discussing other systems and parameters can be found elsewhere in literature [22, 46, 56, 57].

Evolution during the reaction period

The intrawall micropores of materials synthesized using Pluronic as surfactant are formed as a result of the penetration of the poly(ethylene oxide) PEO chains into the silica

framework [58]. Galarneau et al. [59, 60] studied more intensively the micelle structure of SBA-15 hexagonal mesophases created with the block copolymer Pluronic P123. At low temperature (around 60 °C) P123 micelles in water are surrounded by a nearly 1 nm thick corona of hydrated PEO chains. The repulsion between the hydrated PEO chains takes the micelles to a distance of at least 3-4 nm. An increase of the temperature results in a partially dehydration of the PEO chains and in a decreasing volume of the hydrophilic corona. Thereby the core radius of the micelle increases as shown in Figure 2.4. This leads to larger mesopores as a function of increasing temperature.

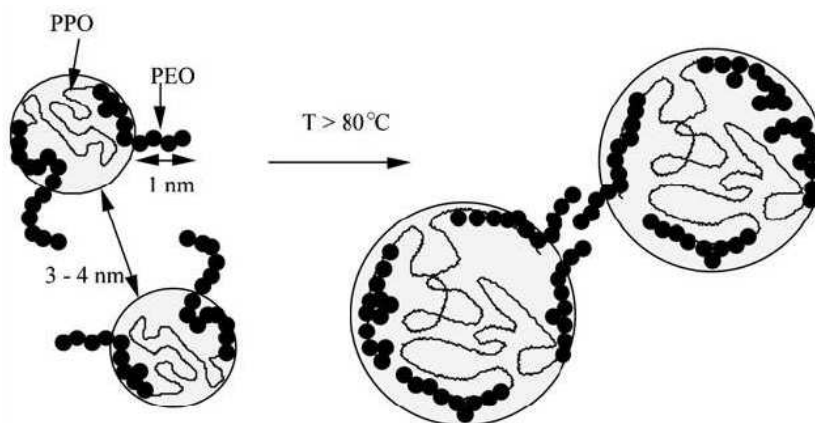


Figure 2.4.: Schematic representation of micelle dehydration with temperature, from Galarneau et al. [60].

On the basis of electron parametric resonance (EPR) and electron spin-echo envelope modulation (ESEEM) experiments using spin-labeled block copolymer templates, Ruthstein et al. [61] proposed a formation mechanism of SBA-15 materials. In Figure 2.5 the initial stages during the formation are shown. The polymerization reaction starts within the first minutes after adding the acid and silica source in the hydrophilic corona region of the solution (stage 2.5a). The decrease in water density (stage 2.5b) lead to an enlargement of the micelle core region and to formation of larger aggregates in stage 2.5c. The silica wall thickness decreases during this process continuously. The PEO chains of the block copolymer surfactant were found to be deeply occluded within the silica wall during this process. As mentioned above these chains are responsible for the generation of the complementary intrawall microporosity. For a detailed discussion of the mechanism refer to the original study from Ruthstein et al. [61].

Evolution during the aging period

During the synthesis of the SBA-16 series in this work and of the SBA-15 series in previous studies Hoang et al. [25] the reaction conditions were kept constant and only the time and temperature during the aging period were varied (see chapter 4).

An increase of the aging temperature results in an increase in the mesopore diameter and in a decrease in the micropore volume, due to the dehydration of the PEO blocks, as

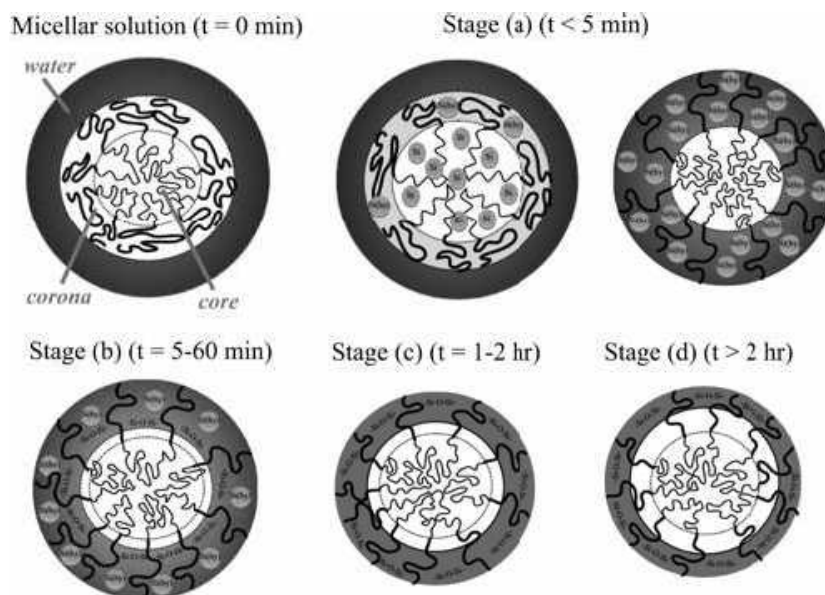


Figure 2.5.: Proposed model for the initial stages in the formation of SBA-15 materials. Darker regions represent a higher concentration of water molecules, from Ruthstein et al. [61]

observed during the reaction period. It is thus relatively easy to tailor these structural properties as a function of the aging temperature. The time of the aging process results in similar effects. The mesopore sizes are increasing and the intrawall micropore volume is decreasing. This is mainly due to a better condensation of the structure as a function of these parameters [62]. The time dependence influences the structure in a linear way whereas the temperature dependence is exponential as can be seen in this thesis or in other recent studies varying these parameters [25, 54].

Galarneau et al. [60] investigated in detail the influence of the aging temperature on the intrawall porosity as well as the connections between micro- and mesopores of SBA-15 materials. In Figure 2.6 a schematic representation of the SBA-15 structure is shown. An aging temperature of 35 to 60 °C (Figure 2.6A) shows only micropores in the silica walls but no interconnections between the mesoporous channels. The micelle corona seems to be too thick for the PEO chains to connect one micelle to another. The first interconnections are generated when the temperature is increased above 80 °C. At 100 °C and higher interconnecting mesopores are formed (Figure 2.6B) and at 130 °C no microporous interconnection between the mesopores are left (Figure 2.6C). For SBA-16 materials this mechanism is likely also to be valid, but it is important to note, that the volume of the micelle corona of the block copolymer Pluronic F127 is greater than the one of Pluronic P123 and thus providing thicker walls and probably more interconnections between the mesopores.

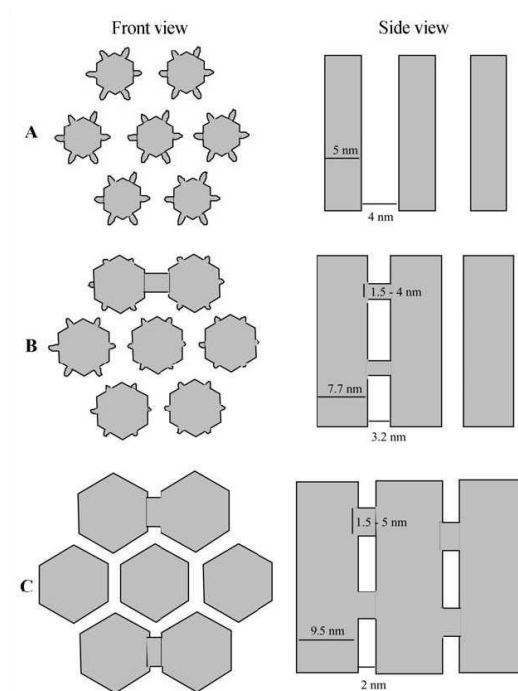


Figure 2.6.: Schematic representation of the pore structure of SBA-15 materials synthesized (A) between 35 and 60 °C, (B) around 100 °C and (C) at 130 °C, from Galarneau et al. [60].

3. Methods and calculations

3.1. Physisorption

A common method for determination of pore volume, pore sizes, areas or volumes is the sorption of probe molecules on a porous solid. Nitrogen or argon physisorption has found to be a generally accepted method for this kind of characterization of porous materials.

The adsorption of a gas on a solid can be quantitatively described by an adsorption isotherm, which represents the amount of condensed molecules (the adsorbates) in a porous solid (the absorbent) as a function of the partial pressure of the gas-phase at a constant temperature. Because of the temperature dependence of sorption in general, it is necessary to measure under isothermic conditions.

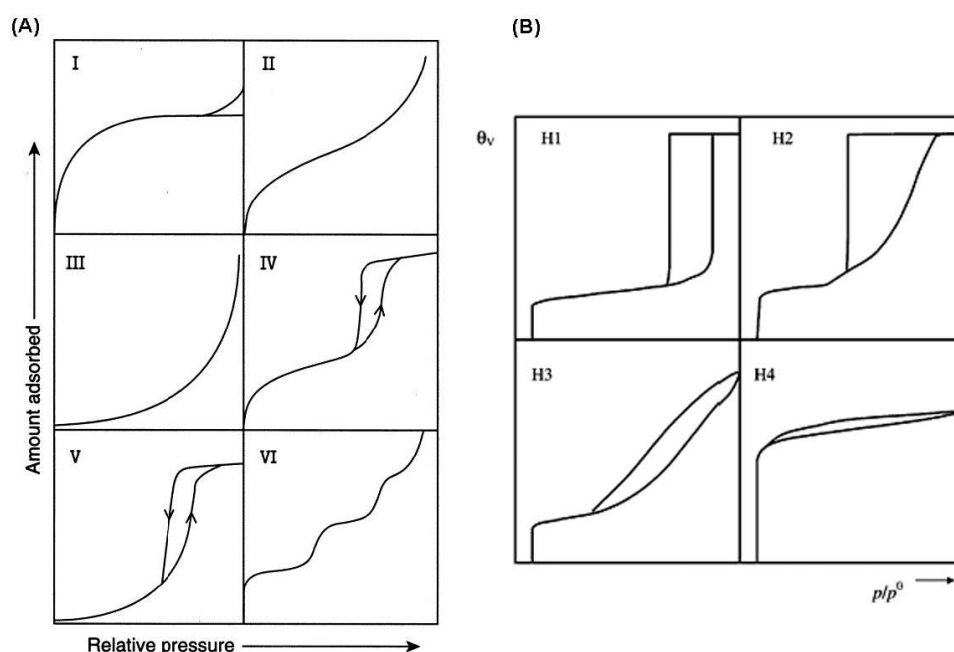


Figure 3.1.: (A) IUPAC classification of sorption isotherms from Sing et al. [1] (1985); (B) Modern classification of hysteresis loops from Rouquerol et al. [63] (1999).

Depending on the structure of the solid and on the forces during adsorption, the IUPAC developed in 1985 a standard classification into six general sorption isotherm types. Type I is characteristic for microporous solids like zeolites or monolayer adsorption, type II for nonporous and type III for macroporous solids. Type IV and V possess a

hysteresis loop typical for sorption in mesopores proceeding through multilayer adsorption and capillary condensation. Type VI represents the relatively rare stepped multilayer sorption isotherm (Figure 3.1A).

Beside the IUPAC classification, the interpretation of the hysteresis loop observed for mesoporous materials with type IV isotherms can reveal more interesting phenomenas. Rouquerol et al. [63] has classified the hysteresis loop into four main types as shown in Figure 3.1B. A loop of type H1 is symmetrical with nearly parallel adsorption and desorption branches and often found in cylindrical pore systems in materials like MCM-41, MCM-48 or SBA-15. Type H2 is asymmetrical and triangular and can be assigned to pore systems with pore network connectivity and pore blocking effect like 'ink-bottle' pores. Type H3 is typical for slit-shaped pores.

It is generally believed that the shape of the adsorption branch of the hysteresis loop is related to the absence or presence of pore network connectivity in the mesoporous materials. Type H1 hysteresis loop is usually assigned to a mesoporous material made up of unconnected pores, whereas type H2 hysteresis loop is expected for mesoporous materials with a connected pore structure [64].

Neimark has shown that three different effects can affect the hysteresis loop. These are in particular cavitation and pore-blocking effects or the near equilibrium desorption. In SBA-15/MCM-41 or MCM-48 materials the desorption is generally near equilibrium, no major kinetic effects are limiting the desorption. In pore-blocked materials such as SBA-16 the desorption is kinetically limited by smaller pore entrances, the desorption can be spinodal, that means at a certain critical point the liquid will switch from an meta-stable regime to an unstable regime and desorp immediately out of the mesopores at a certain pressure. Cavitation effects are similar to pore blocking and also a spinodal desorption occurs, but even at a lower pressure ($0.45 - 0.48 p/p_0$) due to even smaller pore entrance sizes [36, 53].

3.1.1. Theoretical isotherms

Different models were developed to describe the concept of adsorption on a surface. The most popular isotherm models can be classified into models describing monolayer localized adsorption on a flat and energetically homogeneous or heterogeneous surface, in multilayer adsorption isotherms and in isotherms describing the adsorption in micro- and mesopores.

The isotherms describing adsorption on an energetically homogeneous surface like the original Langmuir, the Fowler-Guggenheim or the Kiselev equation follow Henry behavior and reduce to the Henry isotherm at very low concentrations or pressures:

$$\theta(x) = K_H \cdot x, \quad \text{with } x = \frac{p}{p_0} \quad (3.1)$$

where θ represents the dimensionless loading of the adsorbent, x the relative pressure i.e. the fraction of the vapor pressure of the adsorbates p and the saturation pressure of the

pure adsorbates p_0 and K a constant. K describes, in the case of the Henry isotherm, Henry's constant K_H .

Equation (3.1) is the simplest isotherm, describing the linear part of adsorption that may be observed for relatively high temperatures and very low pressures. The slope of this linear region is the dimensionless Henry constant. This adsorption law is formally identical to the well known Henry law for gas absorption in liquids and describes the intrinsic affinity of the adsorbent for a specific sorbate. Defined in this way the Henry constant is an equilibrium constant and shows van't Hoff temperature dependence:

$$K = K_\infty \cdot e^{\frac{-\Delta E_0}{RT}} \quad (3.2)$$

where ΔE_0 represents the change in internal energy or enthalpy of adsorption.

3.1.2. The BET-surface analysis

Brunnauer, Emmett and Teller introduced the concept of multilayer adsorption. Here the first layer of adsorbed molecules acts as new substrate for further adsorption. The classical 2-parameter equation is the well known BET-equation:

$$\theta_{\text{BET}}(x) = \frac{n}{n_m} = \frac{1}{1-x} \cdot \frac{Kx}{1+(K-1)x} \quad (3.3)$$

with the total amount of adsorbates n , the amount of adsorbates in a monolayer n_m , the relative concentration or pressure x and a constant K which is related to the net heat of adsorption of the monolayer. It is important to note that this classical form is only valid for an infinite number of layers on a flat surface taking into account the same heat of adsorption for each layer. To calculate the parameters n_m and K equation (3.3) can be rewritten into the classic BET linear form:

$$\frac{x}{n(1-x)} = \frac{1}{n_m K} (1 + (K-1)x) = \frac{1}{n_m K} + \frac{K-1}{n_m K} x \quad (3.4)$$

Now a plot of $x/n(1-x)$ against x should yield in a straight line in a pressure range of about 0.05 to 0.3 p/p_0 . From the slope and the intercept it is now possible to determine the above two parameters. The specific surface S_{BET} occupied by the monolayer of the adsorbates can be obtained from n_m and the net heat of adsorption from K . Some restrictions to the parameter K can be used to optimize the BET analysis. For instance K always has to be positive and larger than zero. Also it should not be too high or too low. Sing et al. [1] analyzed the influence of K .

The BET equation was implemented in two different ways. The first algorithm tries to find the maximum surface area and to optimize the parameter K in the relative pressure range from 0.06 to 0.15. This leads of course to a variable pressure range from sample to sample, but eliminates erroneous data points in the measurements and yields in more physical consistent values of K . The second way was the strict application of the BET plot in same pressure range as above, but without any more sophisticated algorithm. In appendix B.1 the implementation in Matlab used to calculate these parameters is listed.

The analysis of the adsorption isotherm by the BET method is a common method to determine the surface area of a porous material, but is mostly restricted to mesoporous or macroporous materials. The application of the BET method to materials containing micropores has to be done with care and only an apparent surface area can be obtained.

Other analytical isotherms will not be further discussed here, because they are not relevant for this work.

3.1.3. Micropore analysis

Different methods were established for a quantitative determination of the micropore volume and size. The most direct way is to use probe molecules with varying kinetic diameters as sorbates and to compare their sorption isotherms or to analyze the kinetics of diffusion and sorption.

Other common methods are comparative plots like the t -plot or the α_s -plot method, the Dubinin-Radushkevich (DR), Dubinin-Astakhov (DA), Horvath-Kawazoe (HK), Saito-Foley and methods based on the density functional theory (DFT) [65, 66, 67, 68, 69].

In this section only the comparative plot methods will be discussed. The principle of comparative plots is to compare a physical quantity by plotting two measurements against each other. If the mechanism of change is the same in both measurements, the plot would yield in a straight line. In the case of physisorption data the t -plot method and the α_s -plot have found broad application to determine micropore, mesopore volume, internal and external surface area of micro- and mesoporous materials [31]. Generally the α_s method is more accurate than the t -plot especially for the low and high pressure regions, because it uses a measured reference isotherm.

The following equations were implemented as t -curves in Matlab for the t -plot method. In principle these are type II isotherms, reflecting the statistical thickness of the adsorbed Nitrogen multilayer:

$$t_{\text{Boer}} = 0.1 \cdot 15.47 \cdot \frac{V_{\text{ads}}}{S_{\text{BET}}} \quad (3.5)$$

$$t_{\text{Harkins}}(\text{nm}) = 0.1 \cdot \left(\frac{60.65}{0.03071 - \log x} \right)^{0.3968} \quad (3.6)$$

$$t_{\text{Harkins2}}(\text{nm}) = 0.1 \cdot \sqrt{\frac{13.99}{0.34 - \log x}} \quad (3.7)$$

$$t_{\text{Hasley}}(\text{nm}) = 0.1 \cdot 3.54 \cdot \left(\frac{5}{-\ln x} \right)^{1/3} \quad (3.8)$$

Equation (3.5) is the original t -plot equation by Deboer et al. [68] which gives a relationship of the statistical film thickness and the experimental isotherm. V_{ads} is the adsorption isotherm (STP). Equations (3.6) and (3.7) are both by Harkins and Jura. Equation (3.6) shows a good agreement with experimental data for cylindrical pores and has been used to modify the Kelvin equation in the modified BJH method as developed by Kruk

et al. [70] in 1997. The last equation (3.8) is from Hasley/FHH and is more useful for microporous materials. In this work only equation (3.6) will be further applied if not otherwise specified.

The reference isotherm for the α_s method in this work is Nitrogen on the macroporous silica gel LiChrospher Si-4000 [31, 58] which is also of type II. Stepwise linear interpolation was used for filling the gaps in the reference dataset. Furthermore for all linear curve fitting the variance of the fit was calculated and minimized to ensure a good representation of the linear region.

The presence of micropores is indicated by a positive intercept of a linear fit of the low pressure or the first linear region, of both t - and α_s -plots. It is caused by a relatively large nitrogen uptake at a very low pressures, due to the stronger adsorption in micropores. Hence, it is possible to calculate the micropore volume V_{mi} from the intercept. From the high pressure linear region of the α_s -plot it is possible to determine the external surface area S_{ext} of the porous material. Deviations from linearity are often caused by capillary condensation in mesopores or different types of pores, as for instance slit-shaped pores. Detailed calculations and further interpretation of these methods can be found elsewhere [31, 68].

3.1.4. Pore size distributions

The pore size distribution reflects in some way the distribution of any one dimensional geometric parameter of a porous material. Of course any arbitrary parameter can be used to generate other kinds of distributions, such as pore volume distributions.

Looking at this definition, one easily realizes that the exact description of the porous geometry is fundamental to obtain valid distributions for any geometric parameter of the porous systems.

The typical pore size distribution (PSD) can be obtained in a statistical or in a classical way. The basic concept of the statistical way, which is in parts equal with the thermodynamic way, is to represent the experimental physisorption isotherm as a set of independent, non-connected pores. This can be done by multiplication of the sum of all pore sizes of the system (the actual PSD) with the theoretical representation of the adsorption data, as expressed by the following integral equation:

$$N_{exp}(x) = \int_{R_{min}}^{R_{max}} N_{theo}(x, r) \cdot PSD(r) dr \quad (3.9)$$

where $N_{exp}(x)$ is the experimental isotherm as a function of the relative pressure and $N_{theo}(x, r)$ the theoretical isotherm as a function of the relative pressure and the pore radius (or any other one dimensional geometric parameter of the porous system). To obtain the PSD, this equation has to be solved by inversion of the integral equation.

The main challenge is now to find a appropriate theory to compute the theoretical isotherm. An analytical solution by statistical mechanics and thermodynamics is the (non local) density function theory (NLDF). Also well known are numerical solutions

by Monte Carlo simulations. The classical way is known as the BJH-method and has been developed 1951 by Barrett et al. [71]. It is based on classical thermodynamics and uses the Kelvin equation to calculate the radius of the pore and an adequate analytical equation for the statistical film thickness of the adsorbates. The Kelvin equation is only valid for a limited number of geometries and is a function of the shape. These are for example cylindrical, spherical or slit-shaped mesopores.

Kruk et al. [70] proposed in 1997 a modified version of the BJH method. They introduced a correction term for the original statistical film thickness equation and were able to accurately reproduce the pore size distributions of MCM-41 materials. The original and the modified BJH methods will be further studied in the following section.

The original and modified BJH method

As mentioned before, the original BJH method [71] is based on a model for capillary condensation and evaporation in cylindrical pores using the classical Kelvin equation:

$$\ln x = -\frac{2\gamma V_L}{RT r_c(x)} \quad (3.10)$$

where V_L represents the molar volume of the liquid, γ the surface tension and $r_c = r - t(x)$ with r_c as the 'core' radius and r as the physical radius of the pore. The treatment of 'core' radius and pore radius is the main difference of different BJH methods. The original BJH assumes a constant ratio of 'core' to pore radius.

The Kelvin equation in (3.10) quantifies the deviation in equilibrium vapor pressure above a curved surface from that above a plane surface at the same temperature. In other words, it gives a basic relationship between curvature and thermodynamic activity of a liquid film.

Original BJH method In the original BJH method [71] a calculation scheme has been developed to solve the following integral equation:

$$N_{\text{exp}}(x) = \int_{R_{\min}}^{\infty} \pi \cdot (r - t)^2 \cdot \text{PSD}(r) \, dr \quad (3.11)$$

The calculation scheme can be written the following way:

$$N_{\text{exp}}(x) = \underbrace{\sum_{i=1}^k \Delta V_i(r_i \leq r_c(x_k))}_{\text{1st part}} + \underbrace{\sum_{i=k+1}^n \Delta S_i \cdot t_i(r_i > r_c(x_k))}_{\text{2nd part}} \quad (3.12)$$

or as an indexwise scheme:

$$V_n = \frac{\bar{r}(x_n)^2}{(\bar{r}_{c,n} + \Delta t_n)^2} \cdot \left[\Delta N_{\text{exp}}(x, n) - \Delta t_n \cdot \underbrace{\sum_{j=1}^{n-1} \frac{\bar{r}(x_n)^2}{(\bar{r}_{c,n} + \Delta t_j)^2} \cdot \Delta t_j \cdot \frac{2V_j}{\bar{r}(x_j)}}_{\Delta S_n} \right] \quad (3.13)$$

This recursive defined equation has to be implemented starting 'backward' from the point where all pores are filled up with liquid (the last point of the desorption or adsorption branch). The PSD follows from the above using its definition: $\text{PSD}_n = V_n/2\Delta r_n$. The implementation of the above calculation scheme is listed in appendix B.2.

Modified BJH method (KJS) As stated before the most important difference of the modified BJH method or KJS method [70] is the treatment of the core radius of the kelvin equation. Introducing the statistical thickness and a correction factor, Kruk, Jaroniec and Sajary [70] were able to modify equation (3.10) to better represent the experimental data of SBA-15 measurements. The modified equation to calculate the core radius is the following:

$$r_c(x)(\text{nm}) = \frac{2\gamma V_L}{RT \ln x} + t_{\text{Harkins}}(x) + 0.3 \quad (3.14)$$

3.1.5. Measurements

Nitrogen physisorption isotherms were measured using an Omnisorp-100 static-volumetric sorptometer at liquid nitrogen temperature (77 K). The calcinated samples were first activated under vacuum for 6 h at 250 °C. After the measurements the weight of the samples was determined on an analytical balance at room temperature.

3.2. X-ray diffraction (XRD)

X-ray diffraction (XRD) is an extensively used technique in material science to determine crystallographic and textural properties and inner stress due to defects. Even while ordered mesoporous materials are amorphous materials on a short range scale, the long range order still produces distinct diffraction patterns at angles in the range of $0^\circ < 2\theta < 5^\circ$ when the Bragg conditions are fulfilled.

The Bragg's law states, that at distinct (hkl) planes, a reflection will be observed during X-ray irradiation:

$$n \cdot \lambda = 2 \cdot d_{hkl} \cdot \sin \theta_{hkl} \quad (3.15)$$

where λ is the wavelength of the X-ray beam, θ the so called glancing angle, d the spacing between the (hkl) planes in the lattice and n the order of diffraction ($n \in \mathbb{N}^+$). hkl are the Miller indices.

The unit-cell parameter a of the crystallographic structure was obtained by solving the following equation depending on the type of space group:

$$a = \sqrt{Q_{hkl}} \cdot d_{hkl} \quad (3.16)$$

where Q_{hkl} is:

$$Q_{hkl} = h^2 + k^2 + l^2 \quad (3.17)$$

for a cubic space group like the cubic body centered ($Im\bar{3}m$) SBA-16 or

$$Q_{hkl} = \frac{4}{3} (h^2 + hk + k^2) + \left(\frac{a}{c} \cdot l\right)^2 \quad (3.18)$$

for a hexagonal space group $P6$. In the case of the 2-dimensional SBA-15 or MCM-41 materials with space group $P6mm$, there is no periodicity along the direction corresponding to the c -index.

The exact determination of the space group is often not as straightforward as it might look like. To minimize assumptions and ambiguities of powder X-ray diffraction, the measurements should be accompanied by additional methods such as electron diffraction or microscopy. Also simulations of diffractograms might be very useful. In contrast the determination of the structure using single crystal X-ray diffraction is more reliable, but due to the synthesis process of micro- and mesoporous materials based on silica no single crystal is formed. In this thesis the XRD measurements were accompanied by small angle X-ray scattering and transmission electron microscopy for the confirmation of the $Im\bar{3}m$ symmetry of the SBA-16 series.

The powder X-ray diffraction patterns were recorded with a Bruker D4 powder X-ray diffractometer using Cu-K_α radiation.

Additionally, the powder X-ray diffraction patterns of calcined samples were analyzed with a STOE STADI P θ - θ powder X-ray diffractometer in reflection geometry (Bragg-Brentano) using $\text{Cu-K}_{\alpha 1+2}$ radiation with secondary monochromator and a scintillation detector. XRD patterns were recorded in the ranges of 0.7-2.5 (2θ) with step: 0.1 (2θ), time/step: 10 s.

3.3. Small angle X-ray scattering (SAXS)

Small angle X-ray scattering (SAXS) is a powerful technique to study structural properties on a nanometer length scale in the range from 1 to 300 nanometers. These are typically macromolecules, colloids or for instance mesoporous materials. It is performed by focusing an X-ray beam onto a sample and observing a coherent scattering pattern that arises from electron density inhomogeneities within the sample. A typical SAXS pattern of the SBA-16 sample S-100-2 is shown in Figure 3.2.

The SAXS patterns of the SBA-16 series were acquired on a Nanostar U small-angle X-ray scattering system using Cu-K_α radiation. The d-spacings were calculated directly from the scattering patterns by $d = 2\pi/q$.

3.4. Transmission electron microscopy (TEM)

Transmission electron microscopy (TEM) is a technique whereby a beam of electrons is focused onto a sample (specimen) to create an image of very small structures of materials.

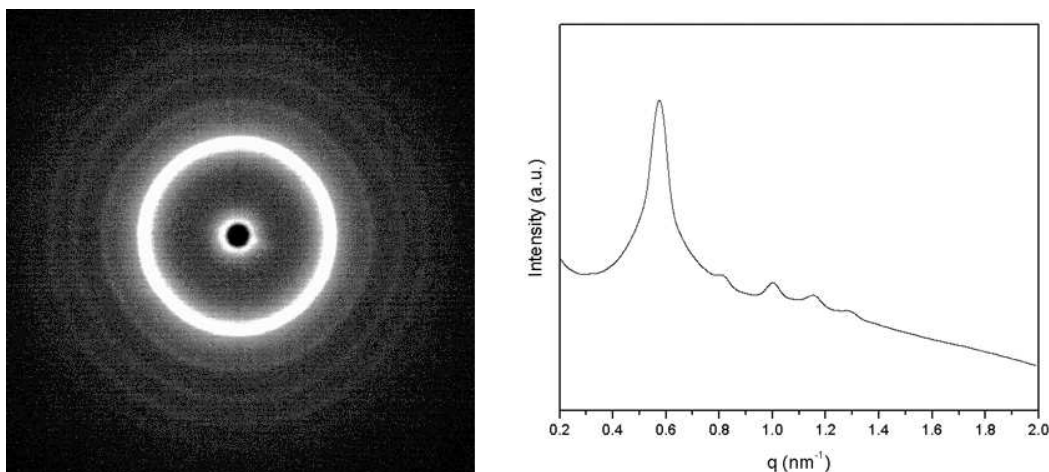


Figure 3.2.: SAXS pattern of SBA-16 sample S-100-2.

In contrast to a classical light microscope, the electron beam interacts mostly by scattering or diffraction rather than absorption, although the intensity of the transmitted beam is still affected by the volume and density of the material through which it passes. The intensity of the diffraction depends on the orientation of the planes of atoms in a crystal relative to the electron beam. At certain angles the electron beam is diffracted strongly, sending electrons away from the axis of the incoming beam, while at other angles the beam is largely transmitted. In the case of SBA-16 materials with a cubic body centered $Im\bar{3}m$ symmetry these orientations are $[100]$, $[110]$ and $[111]$. Furthermore it is possible to determine the position and also the type of defect present, by carefully orientation of the specimen. The resolution of the microscope is only limited by the wavelength (energy) of the electrons, which can be easily tuned by adjustment of the accelerating fields. At present high electron resolution microscopy (HREM) allows separations at atomic scale (0.1 nm).

In this thesis, TEM images of the SBA-16 series were obtained on a JEOL 2011 transmission electron microscope operated at 200 kV. The samples were prepared by dispersing the powder probes in ethanol, then dispersed and dried on a carbon film on a Cu grid.

3.5. Scanning electron microscopy (SEM)

Scanning electron microscopy (SEM) is a powerful technique to study the surface morphologies (texture, shape and size) of the bulk samples of solid materials. A beam of electrons is scanned across the surface of the sample. This method can be combined with energy dispersive X-ray microanalysis (EDX) to analyze the backscattered and secondary electrons produced by the primary beam of electrons. In this thesis, SEM images were used to estimate the size and shape of particles of the samples. The particle size is a critical value to measure effective diffusivity with the zero length column (ZLC) technique.

For all SEM images, a JEOL JSM-840 scanning electron microscope operated at 15 kV was used. The samples were coated by a thin layer of gold before analysis.

3.6. Zero length column (ZLC) chromatography

A number of theoretical and experimental techniques exists nowadays to study diffusion in porous materials. This section gives a brief overview over the zero length column (ZLC) method, which was used to determine the effective diffusivity of several hydrocarbons through the porous structure of selected SBA-16 samples. SBA-15 and Zeolite materials were analyzed recently on the same set-up and the results will be compared in chapter 5 of this thesis. Also a more detailed theoretical study of diffusion in general will be done in chapter 5.

3.6.1. Introduction

As stated before, a number of different techniques exists to analyze the diffusion. Roughly, these methods can be divided in microscopic and macroscopic methods. Figure 3.3 gives an overview over the most important techniques sorted in the range of diffusivities that can be determined by these methods. Only the zero length column will be further discussed here. Detailed descriptions and reviews of the different experimental techniques can be found in the literature.

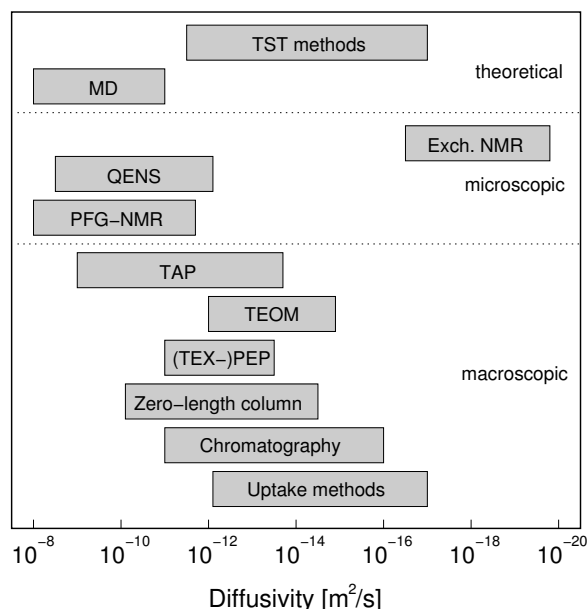


Figure 3.3.: Range of diffusivities that can be determined with different methods. A diameter of 10 μm as assumed for the particle size, from Schuring [72].

The zero length column method uses a very small gas volume which is equilibrated with the sorbate of interest and then purged with an inert gas at a high flow rate in order to further decrease external mass transfer resistances. The experimental set-up and procedure was very similar to the one used by Jiang and Eic [73].

3.6.2. Experimental set-up

The experimental set-up used for the ZLC method in this thesis is shown in Figure 3.4.

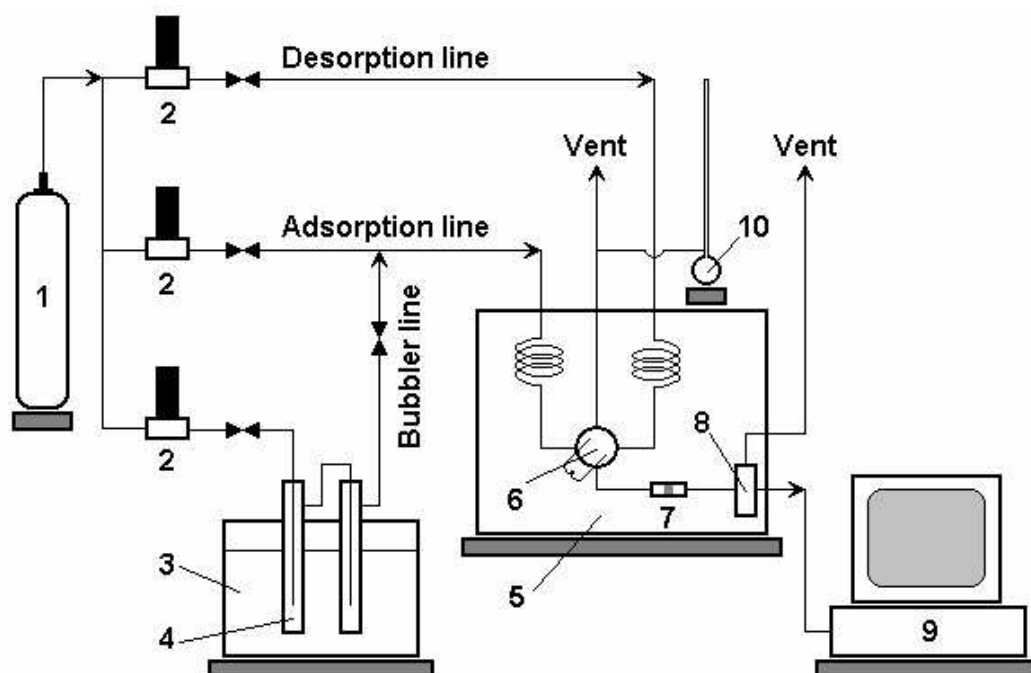


Figure 3.4.: Schematic representation of the experimental ZLC set-up.

The high pressure cylinder (1) contains the Helium inert gas, which was subdivided into three different lines. These are the adsorption, the desorption and the so-called bubbler line. Both adsorption and desorption are high flow rate streams, to minimize external mass resistance during the measurements (see chapter 5). All the flow rates were controlled by mass flow controllers (2). The operating range of the mass flow controllers were 500 ml/min and 10 ml/min for the high and low flow rate line respectively. To achieve a certain concentration of the sorbates in the adsorption stream, the bubbler line was used as a carrier stream and passed through a bubbler (4) containing the liquid hydrocarbons cooled by a thermostat (3) at a constant temperature of $-10\text{ }^{\circ}\text{C}$ to saturate the Helium stream with a certain amount of sorbate. The exact partial pressure of the sorbates is not relevant for the ZLC measurements, it only has to be very low, to be in the linear part of adsorption (see the Henry isotherm). An estimation of the partial pressure can be done using the Antoine equation. Depending on the liquid hydrocarbon sorbates, i.e., n-heptane, mesitylene and cumene, the bubbler flow rate was varied to

control the amount of sorbates in the stream. It is then connected with the adsorption line with a T Swagelok union before passing through the sample. Both desorption and adsorption lines are connected through a 6-way switching valve (6).

The central part of the ZLC system is the zero length cell (7), which consists of a 1/8 Swagelok union. Two 1/8 sintered disks are placed on one end of the union to hold the powder samples between them. The outlet of the ZLC cell is connected to a flame ionization detector FID (8). The 6-way switching valve, ZLC cell and FID detector were placed in a gas chromatograph oven (5) (Hewlett Packard Series II 5890). The reading of the FID was directly transferred and saved (9). Flow rates of desorption and adsorption streams were calibrated using a soap-bubble flow meter (10).

3.6.3. Differential ZLC Model

The basis of the ZLC model is formed by the Fick's second law of diffusion, which describes the mass balance through the solid-phase via diffusion. Mass transfer also occurs via the constant flow through the reactor bed. Both mass balances have to be solved simultaneously. Only the important details of the derivation will be discussed in this section, in appendix A a detailed derivation can be found.

This technique has been applied mainly to gaseous systems [74, 75, 76, 77, 78, 79, 80] but the application to liquid systems have also been reported [81, 82]. The application to zeolite powders has been extended to pellet systems as well. The diffusion of non-hydrocarbon sorbates has been demonstrated. Furthermore, several criterions for ZLC technique were also reported [83, 84, 85, 86, 87].

Model assumptions

The following assumptions were made during the model derivation:

1. The bed is isothermal
2. No external film resistance
3. The adsorption equilibrium isotherm is linear (Henry isotherm)
4. The gas hold-up in the fluid-phase was neglected in comparison with the adsorbed-phase accumulation
5. The particles are spherical and of constant size

Assumptions (1-3) can be controlled and checked during the measurement. This will be discussed in chapter 5. The effect of assumption (4) has to be minimized by a clever design of the set-up. Assumption (5) is more critical. Only taking into consideration the biggest particles, this assumption is good enough for the model. This will be discussed in detail in chapter 5.

Model equations and solution

The mass transfer via diffusion through spherical particles in radial coordinates is given by:

$$\frac{\partial q}{\partial t} = D_{\text{eff}} \cdot \left(\frac{\partial^2 q}{\partial r^2} + \frac{2}{r} \frac{\partial q}{\partial r} \right) \quad (3.19)$$

where q is the concentration of the adsorbed-phase, D_{eff} the effective diffusion constant and r the radial coordinate. The fluid-phase mass balance in one dimension is given by:

$$\frac{\partial c}{\partial t} = D_z \frac{\partial^2 c}{\partial z^2} - c \frac{\partial v}{\partial z} - v \frac{\partial c}{\partial z} - \left(\frac{1 - \epsilon}{\epsilon} \right) \frac{\partial q}{\partial t} \quad (3.20)$$

where c is the concentration of sorbates in the fluid-phase, v the velocity of the fluid ϵ the porosity of the bed, D_z the axial diffusion coefficient and z the axial coordinate. Only taking the relevant terms under assumption of stationarity, under negligence of the fluid-phase hold-up and introducing the volumes of solid-phase one gets (see appendix A):

$$V_s \frac{\partial q}{\partial t} + F \cdot c(t) = 0 \quad (3.21)$$

In this equation V_s is the solid volume and F the fluid flow rate.

Equation (3.19) and (3.20) are a set of coupled differential equations. Brandani and Ruthven presented 1995 an analytical solution to this problem. It can be solved analytically using the above assumptions and initial and boundary conditions (see appendix A). The following set of equations is the analytical ZLC solution for the model and describes the desorption out of a porous 3-dimensional material:

$$\frac{c(t)}{c_0} = \sum_{n=1}^{\infty} \frac{2L}{\beta_n^2 + L(L-1)} \cdot \exp \left(-\beta_n^2 \frac{D_{\text{eff}}}{R^2} t \right) \quad (3.22)$$

$$0 = \beta_n \cdot \cot \beta_n + L - 1 \quad (3.23)$$

$$L = \frac{1}{3} \frac{F}{V_s} \cdot \frac{R^2}{K_H D_{\text{eff}}} \quad (3.24)$$

where R is the mean particle radius, K_H is the dimensionless Henry constant. β_n are the positive roots of equation (3.23) and L a value which introduces the flow rate into the set of equations.

In chapter 5 two different techniques will be implemented to solve these equations. In brief these are the long time analysis and the direct implementation of the above equations.

3.6.4. Measurements

In a typical ZLC measurement, a small amount of the SBA-16 samples (1-2 mg) was placed between the two sintered disks in the ZLC cell and placed inside the chromatograph oven. Then the samples were activated at 270 °C over night for at least 6 hours under

low Helium flow rate. After the activation the two high flow lines were set between 50 and 200 ml/min. Most measurements were done at 100 ml/min. The bubbler flow rate was set to a convenient value in the range of 0 to 5 ml/min.

The adsorption step was maintained until equilibrium conditions were reached, usually this was the case after about one hour. Then the 6-way switching valve was switched to desorption. The relative concentrations (c/c_0) of the effluent sorbates from the ZLC column were determined using a flame ionization detector and transferred to a computer.

By regeneration of the samples at 270 °C over night, several adsorption and desorption cycles could be performed before changing the sample.

3.7. Adsorption of hydrocarbons

3.7.1. Experimental set-up

Sorption equilibrium measurements of n-heptane and toluene on all SBA-16 samples which also were analyzed during the ZLC run and mesitylene and cumene on selected materials were carried out using a digital microbalance (CAHN Instrument, model D-200) connected to a high-vacuum system as shown in Figure 3.5. Sorption measurements of a silicalite reference and of SBA-15 materials were performed on the same set-up in recent studies [88].

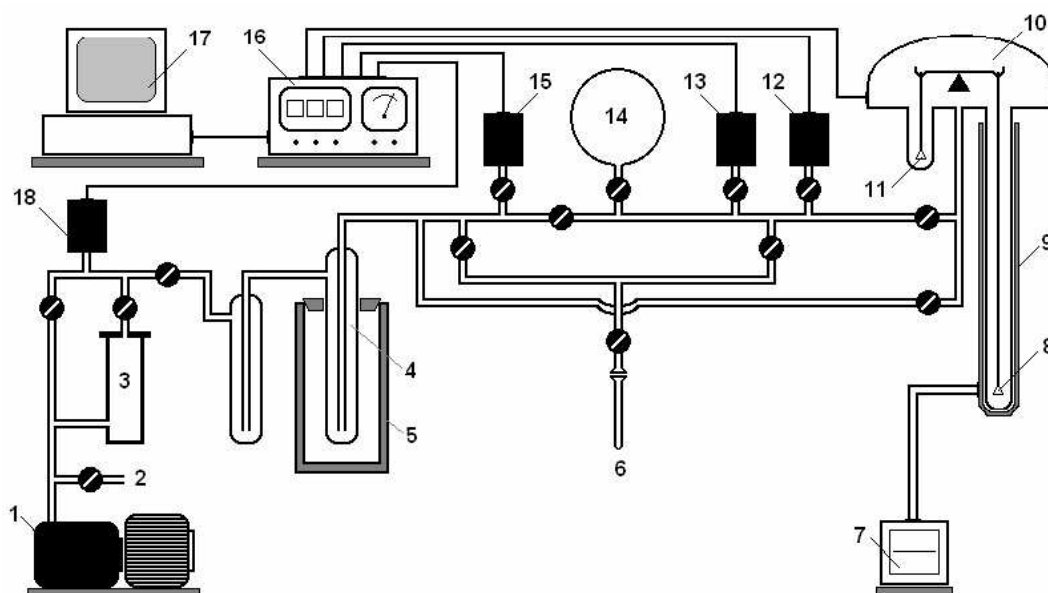


Figure 3.5.: Schematic representation of the experimental sorption set-up.

In a typical run, about 8-10 milligrams of powdered sample was loaded on the sample holder (8). A high vacuum of at least 10^{-3} Pascal of the system was reached by consecutive operating the rotary pump (2) and the oil diffusion pump (3). Under

that pressure, the powder was activated at 270 °C using the heating tape (9) in order to eliminate possible adsorbed impurities and hygroscopic moisture. After at least 6 hours, the sample was cooled down to the required experimental temperature. The electronic balance (10) was used to accurately monitor the weight of the sample. The equilibrium pressure was determined by both pressure transducers (12) and (13) and read on the CAHN D-200 microbalance (16). Adsorption step was started by introducing a dosed amount of hydrocarbon vapor directly to the sample chamber of the electronic balance and recording the weight change after reaching a stable equilibrium pressure. Further consecutive runs were taken by stepwise incrementation of the vapor pressure.

3.7.2. Data analysis and calculations

The adsorption isotherms were obtained from the dependence of adsorption capacities expressed in millimol of sorbate per gram of sample or in cm³ of liquid sorbate per gram of sample with equilibrium pressure p or relative pressure p/p_0 respectively. The maximum adsorption capacities Q (mmol/g) were assumed as the maximum value of sorbate loading in the adsorption isotherms. The Henry constants K_H were calculated from the linear part of the isotherm at very low pressures. The concentration of sorbate was calculated by assuming that the density of the silicate powder is 2.2 cm³/g. The isosteric heats of adsorption H_{ads} of the sorbates on the samples were derived from the temperature dependence of adsorption data, using the Clausius-Clapeyron equation for an ideal gas-phase:

$$\left(\frac{\partial \ln p}{\partial 1/T} \right)_q = \frac{\delta H_{\text{ads}}}{R} \quad (3.25)$$

where p is the equilibrium pressure at absolute temperature T at constant adsorbed concentration q and R is the gas constant.

4. Synthesis and characterization

4.1. Synthesis of SBA-16 materials

A series of SBA-16 materials was synthesized exactly as reported recently by Kim et al. [21], Kleitz et al. [23] using poly(ethylene oxide)-poly(propylene oxide)- poly(ethylene oxide) triblock copolymer in a ternary copolymer-butanol-water system and low-acid concentrations [21, 22, 24]. The aqueous mixture of Pluronic F127 copolymer (EO₁₀₆PO₇₀EO₁₀₆) with Butanol (1-Butanol, Aldrich 99%) was used to create a mesostructure to achieve an ordered self-assembly of the silica source tetraethyl orthosilicate (TEOS, Aldrich 98%).

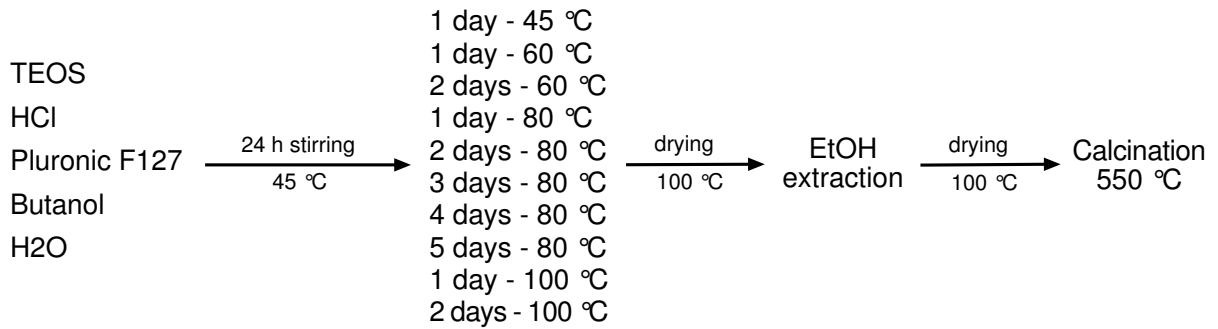


Figure 4.1.: Schematic representation of the synthesis route.

In a typical synthesis 3 g of the copolymer F127 was dissolved in a solution of 144 g distilled water and 5.94 g of concentrated hydrochloric acid (HCl, Fischer 36.5 - 38.0%). After about 20 to 30 minutes 9 g of the co-surfactant Butanol was added, to achieve a 1:3 F127:BuOH mass ratio in the ternary system as shown in Figure 2.1. After 1 hour of stirring 14.2 g TEOS was added to the solution. At a constant temperature of 45 °C the mixture was further stirred for 24 h. The mixture was then placed under static conditions at varying temperatures and times for hydrothermal treatment. The temperature varied from 45 °C to 100 °C and the time from 1 to 5 days depending on the specific sample. After the hydrothermal treatment the precipitated solid was isolated by filtration and dried without any additional washing process at 100 °C for at least one day. The template was removed by a brief extraction in an acidic ethanol solution and further by calcination at 550 °C under air for 6 h. The samples are denoted as S-*T*-*t* with the time *t* between 1 and 5 days and the temperature *T* in the range from 45 °C to 100 °C. For instance, the sample treated for one day at low temperature, is denoted as S-45-1.

4.2. Results and Discussions

4.2.1. Morphology

The morphology of the SBA-16 samples was determined by analysis of the SEM micrographs. The calcinated powder samples were first treated in a sedimentation step to narrow the particle size distributions. Only the relevant samples for the later diffusion measurements were treated this way. The corresponding SEM micrographs of the sedimentation fractions are shown in Figure 4.2.

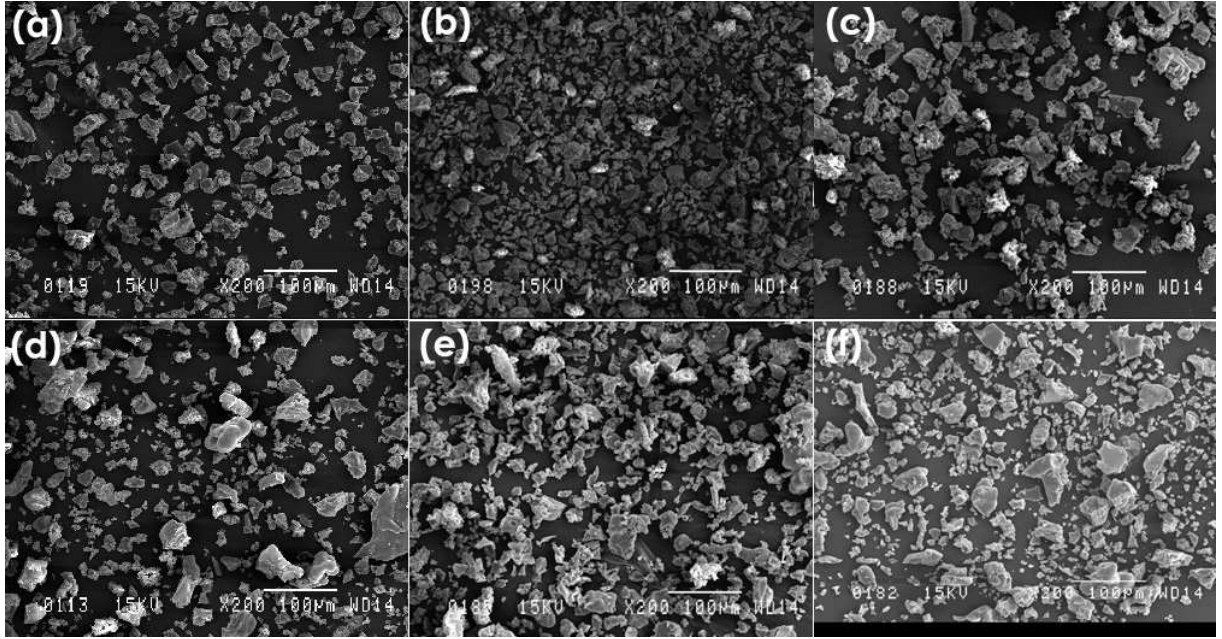


Figure 4.2.: SEM images of SBA-16 samples powder after a sedimentation step: (a) S-45-1 2nd fraction; (b) S-60-1 3rd fraction; (c) S-80-1 2nd fraction; (d) S-80-5 2nd fraction; (e) S-100-1 2nd fraction; (f) S-100-2 2nd fraction.

The estimated particle radii from these micrographs are summarized in table 5.1. The smaller particle size obtained for the sample S-60-1 is due to the different sedimentation fraction. The increasing particle size as a function of temperature or time can be related to the faster particle growing at higher temperatures or the longer aging time resulting in bigger particles.

4.2.2. Crystallographic structure

For determination of the structure and symmetry of the materials, XRD and SAXS patterns and TEM images were analyzed. The reflections of the XRD patterns could be indexed to the cubic body centered space group $Im\bar{3}m$, thus providing an indication of the $Im\bar{3}m$ IW-P structure of SBA-16. The positions of the reflections were confirmed by SAXS measurements.

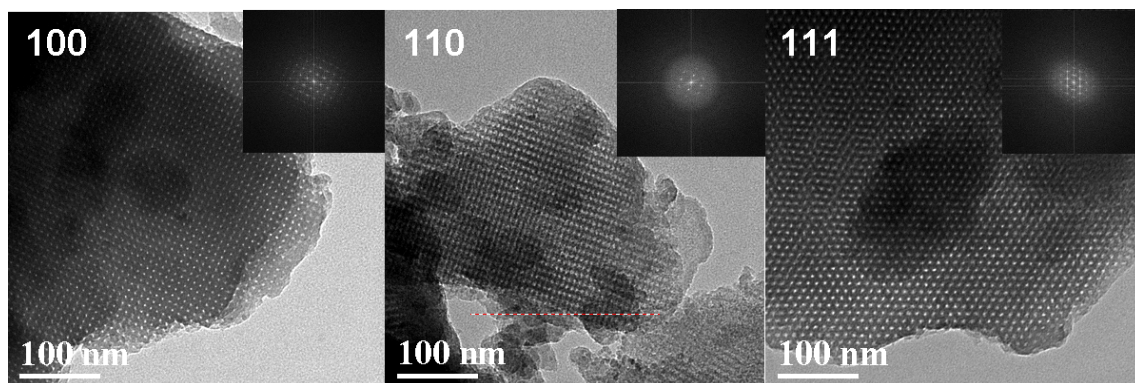


Figure 4.3.: TEM images of sample S-45-1 and their Fourier diffractograms along the [100], [110] and [111] projections of the $Im\bar{3}m$ structure

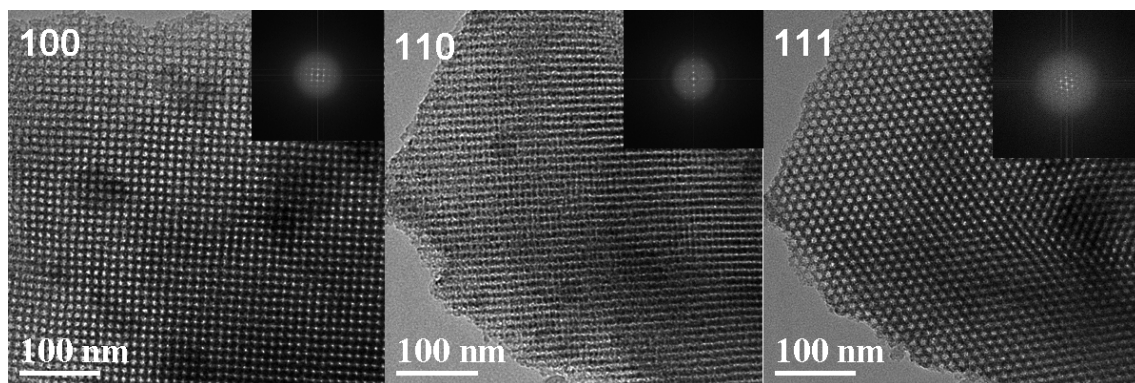


Figure 4.4.: TEM images of sample S-100-1 and their Fourier diffractograms along the [100], [110] and [111] projections of the $Im\bar{3}m$ structure

In Figures 4.5 and 4.6 the XRD and SAXS patterns of representative samples are shown respectively. The augmentation of the hydrothermal treatment time and temperature caused a pronounced shift towards lower angles, an evidence for the enlargement of the unit cells as a function of temperature and time. The shift toward lower angles was accompanied by changes in the relative intensities in the XRD and SAXS reflections. The (200) reflection could be well resolved by SAXS for all samples, but its relative intensity significantly decreases while the higher reflections tend to increase. This behavior could

also be observed by XRD, although the (200) reflection was difficult to resolve for samples with larger unit-cell parameters. This effect can be assigned to the relative change in the pore size to wall ratio and was also recently observed in the case of a mesoporous material with $Ia\bar{3}d$ symmetry by Kim et al. [21]. TEM measurements yielded a confirmation of the $Im\bar{3}m$ symmetry.

Figures 4.3 and 4.4 show images corresponding to [100], [110] and [111] projections of the cubic body-centered ($Im\bar{3}m$) structure for the samples S-45-1 and S-100-1 and their corresponding Fourier diffractograms. The $Im\bar{3}m$ space group is therefore reliably identified. Large domains of highly ordered materials are visible. The change in structural properties could also be confirmed by TEM. Even if it is not possible to directly access the primary mesopore diameter or the pore wall thickness by TEM, it is obvious from Figures 4.3 and 4.4 that for sample S-45-1 the ratio of void to silica wall volume is lower than in sample S-100-1.

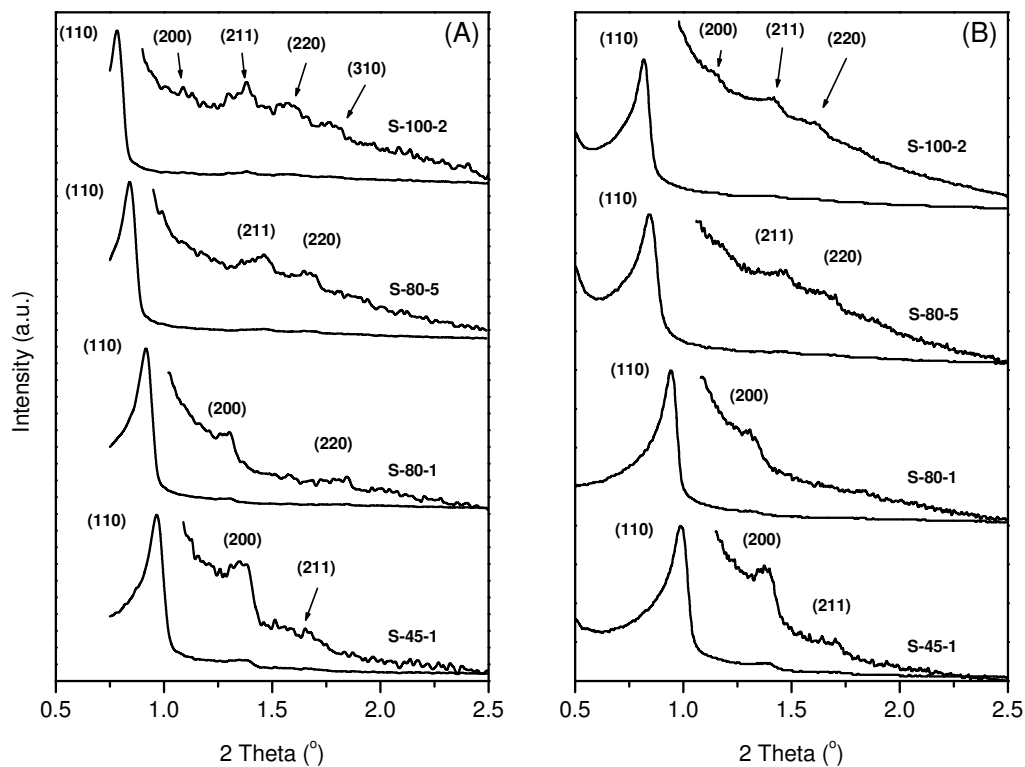


Figure 4.5.: XRD patterns for SBA-16 materials; (A) recorded on a STOE STADI θ - θ powder X-ray diffractometer in reflection geometry; (B) recorded on a Nanostar U small-angle X-ray scattering system.

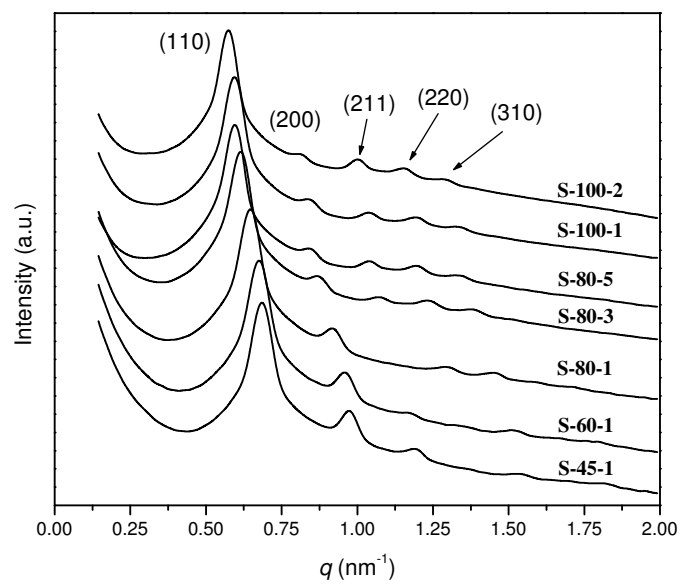


Figure 4.6.: SAXS patterns for SBA-16 materials.

4.2.3. Mesoporous properties

The nitrogen physisorption isotherms of the complete series are plotted in Figure 4.7 showing the shifted isotherms in a normal and semi-logarithmic scale. All the isotherms are of type IV according to IUPAC classification with a triangular hysteresis loop of type H2 typical for materials with ink-bottle pores and pore network connectivity like SBA-16 [1, 47, 53]. Since the evaporation of the fluid always occurs spontaneously and at the same relative pressure of 0.45 to 0.48 p/p_0 , as a result of cavitation [52, 53], the pore entrance diameter to the main mesoporous cavities must be less than 4 nm [53, 54].

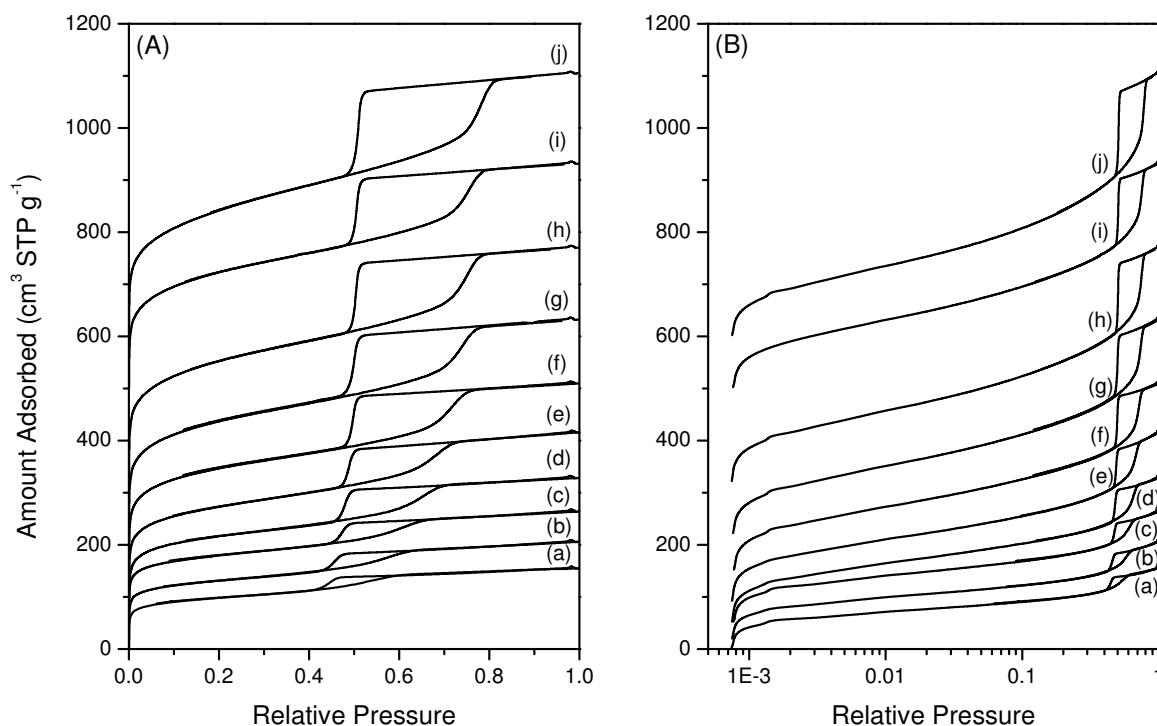


Figure 4.7.: N₂ adsorption-desorption isotherms for SBA-16 materials synthesized at different hydrothermal treatment time and temperature in linear (A) and semi-logarithmic (B) scale. The isotherms (a) S-45-1, (b) S-60-1, (c) S-60-2, (d) S-80-1, (e) S-80-2, (f) S-80-3, (g) S-80-4, (h) S-80-5, (i) S-100-1, (j) S-100-2 are shifted by 0, 20, 50, 50, 90, 150, 220, 320, 500 and 600 cm³ STP g⁻¹ respectively

Varying the hydrothermal treatment time or temperature results in a variation of the total amount of adsorbed nitrogen (estimated at $p/p_0 = 0.99$) and therefore the total pore volume V_t (Table 4.1). The temperature dependence, in the range investigated in this work, is for most properties like maximum adsorbed amount of nitrogen, primary pore size and unit cell size exponential, whereas the time dependence is, as expected, linear. Sample S-45-1 synthesized at low temperature only adsorbs about 0.23 cm³ liquid nitrogen per gram. In contrast, the sample S-100-1 synthesized at high temperature

adsorbs nearly three times more. The hysteresis loop increases in height and width with time and temperature and the capillary adsorption step shifts to higher relative pressures. This is a clear indication for an increasing primary mesopore size and volume. Pore size distributions determined using the BJH-methods are not accurate for materials with non-cylindrical and cage-like pore structures. However, in order to compare this series with recent works on cage-like materials pore size distributions (PSDs) were calculated using the modified BJH method on the adsorption isotherm (see Figure 4.7). The values at maximum of the DBJH are therefore reported in Table 4.1.

Samples	S_{BET} (m^2g^{-1})	V_t (cm^3g^{-1})	a (nm)	D_{BJH} (nm)	D_{me} (nm)	h_w (nm)	ϵ_{me} (-)
S-45-1	370	0.23	12.8	5.2	7.8	8.4	0.24
S-60-1	414	0.28	13.0	5.7	8.3	7.2	0.28
S-60-2	481	0.32	-	6.1			0.30
S-80-1	621	0.42	13.3	6.9	9.2	5.8	0.34
S-80-2	678	0.50	-	7.3			0.40
S-80-3	728	0.55	14.4	8.3	10.5	5.1	0.41
S-80-4	800	0.63	-	8.9			0.44
S-80-5	843	0.68	14.9	9.3	11.4	4.4	0.46
S-100-1	821	0.66	14.9	9.4	11.3	4.4	0.46
S-100-2	886	0.77	15.5	10.4	12.2	3.9	0.51

Table 4.1.: Structural Properties of SBA-16 materials.

For a better evaluation of important geometric properties the Model of Spherical Cavities [53] (MSC) was applied to the materials. In this model the diameter the spherical cavities D_{me} may be calculated as:

$$D_{\text{me}} = a \left(\frac{6 \epsilon_{\text{me}}}{\pi \mu} \right)^{1/3} \quad (4.1)$$

where a is the cubic cell parameter, μ is the number of cavities per unit cell which is equal to 2 for the $Im\bar{3}m$ of SBA-16 and ϵ_{me} is the void fraction associated with the mesopores estimated as:

$$\epsilon_{\text{me}} = \frac{\rho_v V_{\text{me}}}{1 + \rho_v V_{\text{me}}} \quad (4.2)$$

where V_{me} is the specific volume of the cavities calculated by the α_s -plot method and ρ_v the density of the solid walls, which was assumed to be 2.2 g/cm^3 . The average wall thickness can be calculated as:

$$h_w = \frac{2a^3}{\pi D_{\text{me}}^2 \mu} - \frac{D_{\text{me}}}{3} \quad (4.3)$$

The values of V_{me} , ρ_v and ϵ_{me} are also reported in Table 4.1.

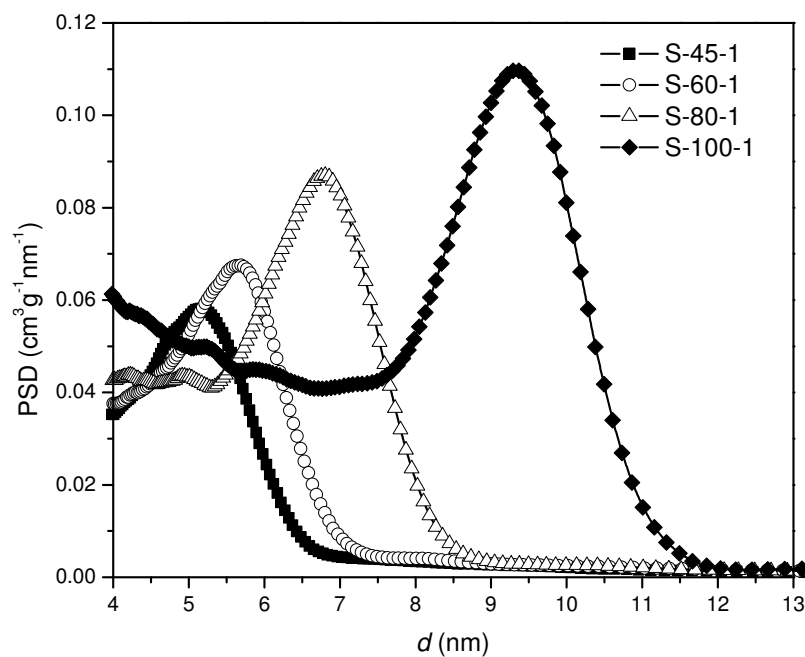


Figure 4.8.: Modified BJH pore size distributions for SBA-16 samples under variation of synthesis temperature.

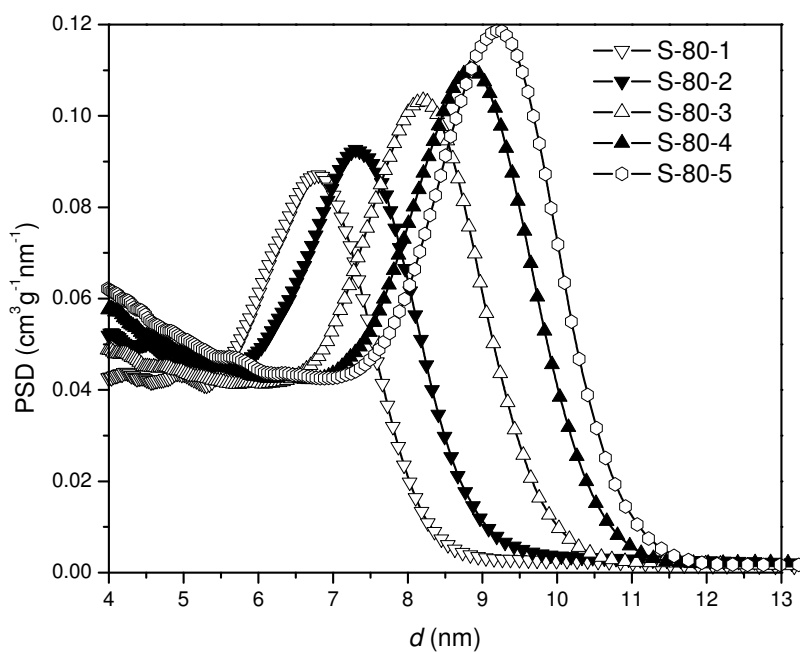


Figure 4.9.: Modified BJH pore size distribution for SBA-16 samples under variation of synthesis time.

4.2.4. Microporous and intrawall properties

As observed in recent studies on SBA-16 materials [54] the comparative methods like t -plot or α_s -plot do not show the usual regular shape below the capillary condensation pressure. As can be seen from Figure 4.10, two different linear regions were observed below the capillary condensation step in the α_s -plot.

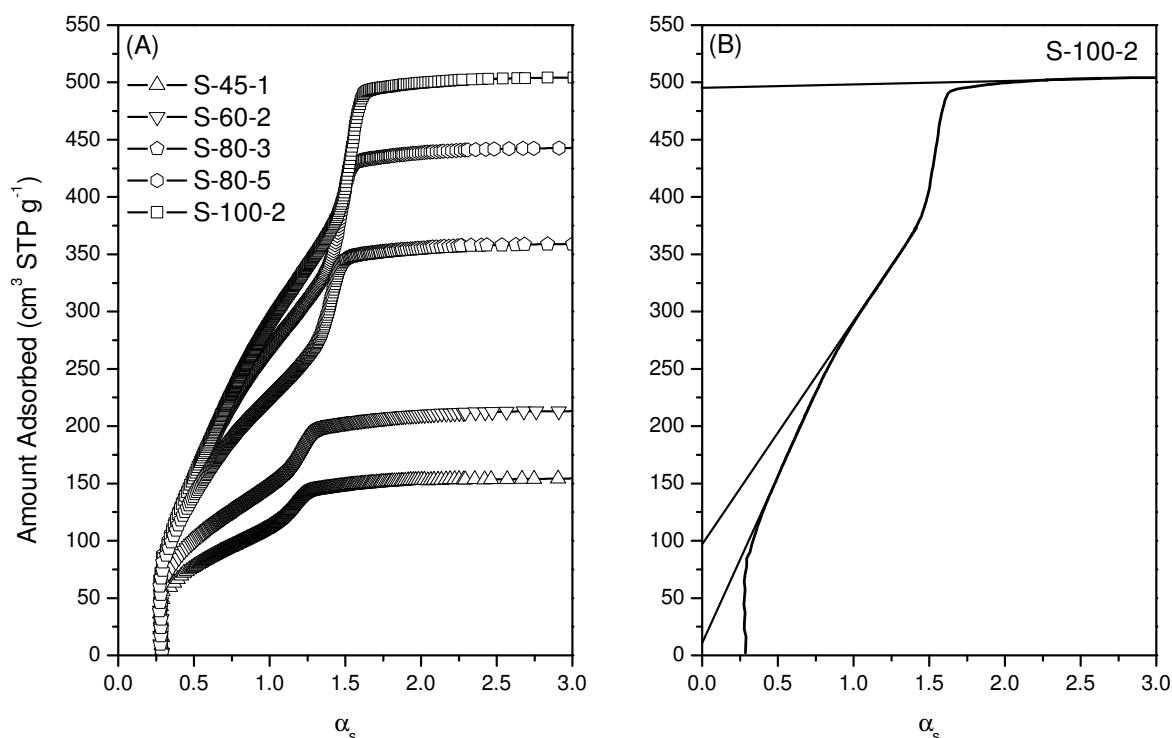


Figure 4.10.: α_s -plot of selected SBA-16 samples.

The low α_s linear region intercept with the ordinate axis yields a volume of micropores (V_1) which is unambiguously ascribed to intrawall micropores. The second linear part intercept yields a sum ($V_1 + V_2$) where V_2 is the volume of a population of small mesopores. The measured values of V_t , V_1 and V_2 are reported in Table 4.2. Interestingly, the experimental values of ($V_t - V_1 - V_2$) are very close to the mesopore volume estimated using the modified BJH approach. The variations of V_1 and V_2 as functions of V_t are shown in Figure 4.11. The nature of the mesopores associated with volume V_2 is difficult to assess as these could not uniquely be intrawall mesopores like those reported in materials synthesized with Pluronic type surfactants [25, 60, 89, 90, 91]. There is also a certain possibility that the volumes associated with the pore apertures linking the primary mesopore cavities may contribute to V_2 . However, since the α_s -plot is drawn from the adsorption branch of the isotherms this second hypothesis is thought less likely. Indeed, in sample S-45-1 that it is believed to be without intrawall mesopores, the volume of V_2 is essentially zero indicating that, at least in this sample, the contribution of the pore apertures is also close to zero.

Samples	V_t (cm ³ g ⁻¹)	V_1 (cm ³ g ⁻¹)	V_2 (cm ³ g ⁻¹)	$V_{me}^{(a)}$ (cm ³ g ⁻¹)	$V_{me}^{BJH(b)}$ (cm ³ g ⁻¹)
S-45-1	0.23	0.072	0.001	0.16	0.18
S-60-1	0.28	0.071	0.005	0.20	0.23
S-60-2	0.32	0.081	0.010	0.23	0.25
S-80-1	0.42	0.101	0.021	0.30	0.33
S-80-2	0.50	0.086	0.031	0.38	0.39
S-80-3	0.55	0.076	0.064	0.31	0.43
S-80-4	0.63	0.060	0.087	0.48	0.49
S-80-5	0.68	0.045	0.110	0.52	0.53
S-100-1	0.66	0.047	0.100	0.51	0.51
S-100-2	0.77	0.018	0.132	0.62	0.61

Table 4.2.: Pore volumes of SBA-16 materials.

Moreover, the consideration of Figure 4.11 also suggests that V_2 is associated with a population of intrawall small mesopores. In this figure it is seen that both V_1 and V_2 increase at $V_t < 0.42$ cm³g⁻¹. This 0.42 value corresponds to S-80-1 which means that below 80 °C the materials have a very large volume of intrawall mesopores. Above 80 °C the contribution of the micropores to the overall pore volume decreases drastically whereas the V_2 value increases steadily. In a recent paper Fajula and Ryoo have established that in SBA-15 the intrawall interconnecting mesopores are created by the growth and enlargement of intrawall micropores [60]. They have specifically pointed out the temperature of 80 °C as the one at which this transition starts occurring. As a consequence we believe that the data in Figure 4.11 reflect the same kind of transition with the conversion of intrawall micropores into (connecting) intrawall mesopores occurring at a significant rate at temperatures equal or higher 80 °C. The interconnected nature of the mesocage pore system of SBA-16 prepared at 100 °C has recently been evidenced independently through the nanocast preparation of CMK-type mesoporous carbon inverse replicas [92].

It should be noted that the slopes of $V_1(V_t)$ and $V_2(V_t)$ at high V_t are essentially equal, amounting to -0.296 and 0.330 for V_1 and V_2 respectively. This strongly suggests that the creation of intrawall mesopore is not by enlargement of a micropore but rather by the coalescence of micropores since at high V_t , $V_1 + V_2$ is a constant.

Assuming the main process is through coalescence of two micropores it is possible to use the data in Table 4.1 and 4.2 to estimate a micropore size.

Indeed the values of specific surface area associated with the primary mesopores may be estimated as:

$$S_x = S_{BET} - S_1 - S_2 \quad (4.4)$$

In the case of cylindrical micropores, the pore areas S_1 and S_2 can be calculated from the pore volumes using a simple geometric relation:

$$S_i = \frac{2V_i}{r_i}, \quad \text{with } i = 1, 2 \quad (4.5)$$

CHAPTER 4. SYNTHESIS AND CHARACTERIZATION

If the small mesopores are obtained by mere coalescence of two cylindrical micropores of radius r_1 then

$$r_2 = \sqrt{2} \cdot r_1 \quad (4.6)$$

and S_x may be expressed as:

$$S_x = S_{\text{BET}} - \frac{2}{r_1} \left(V_1 + \frac{1}{\sqrt{2}} V_2 \right) \quad (4.7)$$

A specific volume of primary mesopores can be in turn estimated as:

$$V_x = \frac{S_x D_{\text{me}}^{\text{BJH}}}{4} \quad (4.8)$$

Samples	r_1 (nm)	dr^* (nm)	S_1 (m^2g^{-1})	S_2 (m^2g^{-1})	S_x (m^2g^{-1})	V_x (cm^3g^{-1})
S-45-1	0.60	0.05	240	2.3	126	0.163
S-60-1	0.60	0.05	237	12	154	0.219
S-60-2	0.60	0.05	270	23	188	0.286
S-80-1	0.55	0.05	404	60	157	0.270
S-80-2	0.50	0.05	346	89	243	0.443
S-80-3	0.45	0.05	337	202	189	0.392
S-80-4	0.40	0.02	300	310	190	0.422
S-80-5	0.40	0.02	225	393	223	0.518
S-100-1	0.40	0.01	235	357	229	0.538
S-100-2	0.35	0.01	102	538	246	0.639

Table 4.3.: Fitting procedure to estimate the micropore radius. * the error bars in Figure 4.12 indicate estimates of $r = r_1 \pm dr$.

Table 4.3 shows the values calculated for S_1 , S_2 , S_x and V_x . In order to fit V_x with the values of $V_{\text{me}}^{\text{BJH}}$ reported in Table 4.2, it was necessary to assume that the micropore diameters were not the same in all samples. The values of r_1 adopted in these calculations are also reported in Table 4.3. In Figure 4.12 the graph of V_x (Table 4.3) as a function of $V_{\text{me}}^{\text{BJH}}$ (Table 4.2) is showing relatively good agreement between these two estimates and justifies the fitting values adopted for the micropore radius (r_1). The error bars in Figure 4.12 correspond to estimates of the micropore radius $r = r_1 \pm dr$ with the values of dr also represented in Table 4.3. The values of r_1 in Table 4.3 are indeed indicating that this parameter depends on temperature, varying from 0.6 nm at 45 °C to 0.35 nm at 100 °C. This suggests that at the lower temperature the PEO chains of the surfactant are to some extent entangled when entrapped in the forming wall. At higher temperature they get less entangled yielding narrower (and possibly longer) micropores.

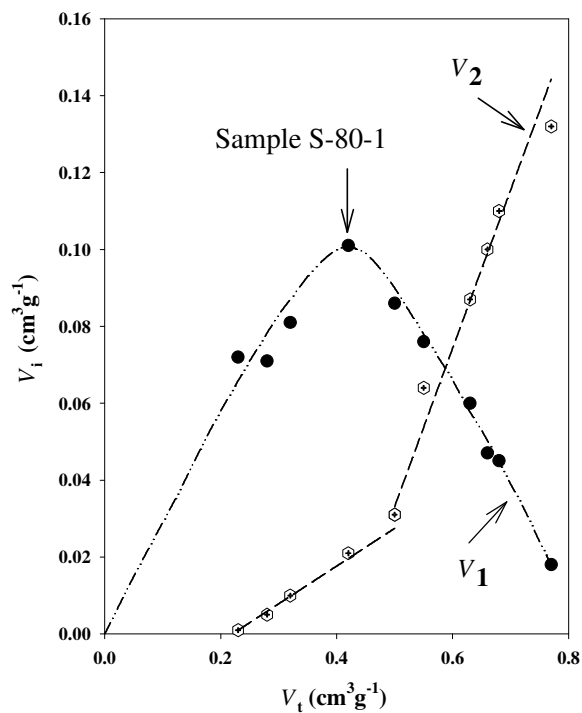


Figure 4.11.: Plots of V_1 and V_2 as functions of the total pore volume for SBA-16 materials.

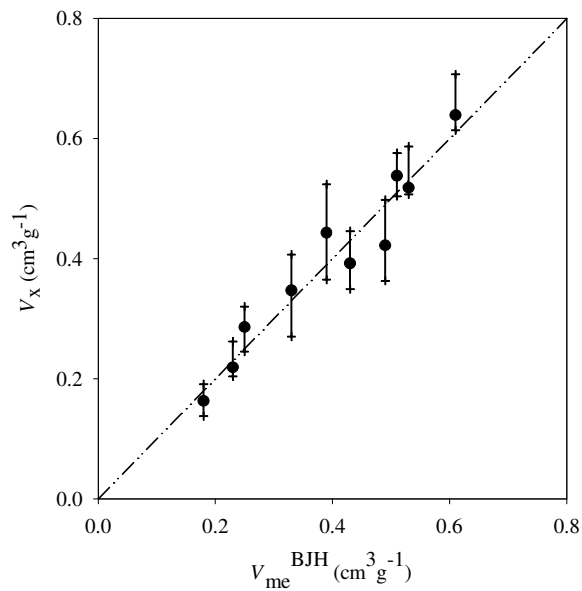


Figure 4.12.: Plot of V_x as a function of $V_{\text{me}}^{\text{BJH}}$ for SBA-16 materials as a confirmation of the fitting values of Table 4.3

4.3. Conclusions

A series of high-quality SBA-16 materials was prepared with different structural properties focusing on the systematic control of intrawall porosity. The mesophase was created using butanol as cosolute. The symmetry and the high quality of the samples was established from XRD, SAXS and TEM measurements. By varying the hydrothermal temperature and time, materials with a high fraction of intrawall micropores and thick wall (S-45-1) up to mesoporous materials with few micropores, thinner walls and large primary mesopores (S-100-2) could be obtained. Using the α_s -plot, it was possible to distinguish two different types of intrawall pores. Moreover the variations in intrawall pore volumes allowed to suggest that the intrawall small mesopores are generated by the coalescence of two micropores, this process happening at a significant rate at temperature exceeding 80 °C. These data also allowed a rough estimate of the micropore radius which varies from 0.6 nm at 45 °C to 0.35 nm at 100 °C. The Model of Spherical Cavities [53] allowed to calculate provided estimates of the primary mesopore size, pore wall thickness and primary mesopore void fraction, which are important structural properties for the correct evaluation of diffusion results. These will be reported in the next chapter of this thesis.

5. Diffusional properties

5.1. Theory

In the case of uniform spherical particles being in linear adsorption equilibrium at very low partial pressures of the sorbate under negligence of the hold-up in the ZLC-bed and assuming perfect mixing throughout the ZLC cell the normalized effluent sorbate concentration c/c_0 is described by the set of equations (3.22 - 3.24).

By fitting this set of equations against the experimental data in the complete time range, it is possible to calculate the effective diffusion time constant D_{eff}/R^2 . However to minimize particle size distribution effects which only appear at short times [83], the so-called long-time solution is more accurate. It is obtained by neglecting all the higher order terms of the sum in equation (3.22) [93] and yields to a straight line on a semi logarithmic plot of the normalized effluent sorbate concentration versus the time. From the slope:

$$m = -\beta_1^2 \frac{D_{\text{eff}}}{R^2} \quad (5.1)$$

and the intercept:

$$i = \frac{2L}{\beta_1^2 + L(L-1)} \quad (5.2)$$

of the plot and under consideration of equation (3.23) the effective diffusion time constant is obtained. The implementation of the long-time solution in Matlab is listed in appendix B.3.

5.2. Measurements and calculations

The ZLC set-up was described in detail by Jiang and Eic [73]. The ZLC column and switching valve were placed in a gas chromatograph oven (Hewlett- Packard Series II 5890). The flow rates were controlled by mass flow controllers.

A small amount of the SBA-16 sample powder (1-2 mg) was loaded into the ZLC column and activated at 270 °C overnight or for at least 6 hours to eliminate possible impurities and moisture in particular. Helium of 99.95% purity was used as the inert carrier gas. n-heptane, cumene or mesitylene (99% grade, Aldrich) were kept in the bubbler, and its vapor was carried by a small flow of helium before being diluted in the main He stream. The sorbate concentration was adjusted and maintained at a low level corresponding to the linear region of the adsorption isotherm (Henry's law region) [77].

In the adsorption step, the samples were equilibrated with sorbate diluted in a helium flow, for about one hour. Then desorption was performed with helium at a flow rate high enough to minimize external mass and heat resistances on the surface of the sample. A flow rate of 100 cm³/min was chosen as standard flow rate for all samples. Flow rates of 100 to 200 cm³/min were chosen to verify the kinetically controlled desorption process. The relative concentrations (c/c_0) of the effluent sorbates from the ZLC column were determined using a flame ionization detector. The desorption was then performed until the baseline was reached or nearly reached.

The effective diffusivity was calculated from the kinetically (diffusion) controlled long-time region of the ZLC curve using up to eight terms of the sum in equation (1). Equilibrium and kinetic limitations were determined by plotting the ZLC-curves (c/c_0) measured at different flow rates against the product of flow rate and time (Ft). Diverging curves signify a kinetically controlled process [94]. The linear conditions of the system (Henry’s law region) were determined by varying the sorbate concentration. The diffusional activation energies were calculated by Arrhenius plots of the corresponding effective diffusivities measured at different temperatures. From SEM images the particle dimensions of the powder samples were obtained.

5.3. Results and Discussions

The results from the long-time analysis of the diffusion measurements are summarized in Table 5.1. As stated in the previous section the time range of the kinetically controlled long-time region was obtained by Ft -plots. In Figure 5.1 Ft -plots for n-heptane and cumene diffusion measurements in S-100-2 are displayed. In Figure 5.2A the desorption curves corresponding to the Ft -plot for n-heptane is plotted. S-100-2 is the sample with the fastest desorption and most likely in an equilibrium limitation². For most samples the short-time region was generally equilibrium controlled, but even for S-100-2 the long time region shows diverging curves and is thus being kinetically controlled. The effective diffusion time constants (D_{eff}/R^2) were in a small error range the same for all flow rates investigated in this work confirming the kinetically controlled regime. In Figure 5.2B the effect of varying sorbate concentration is shown. The slope of the long time region is the same for both measurements, thus indicating that the system is being under linear conditions. The experimental and long-time fittings for the selected samples of the SBA-16 series are presented in Figure 5.3. It was impossible to fit the short- and long-time region simultaneously very likely because of particle size and shape distribution effects of the sample powders.

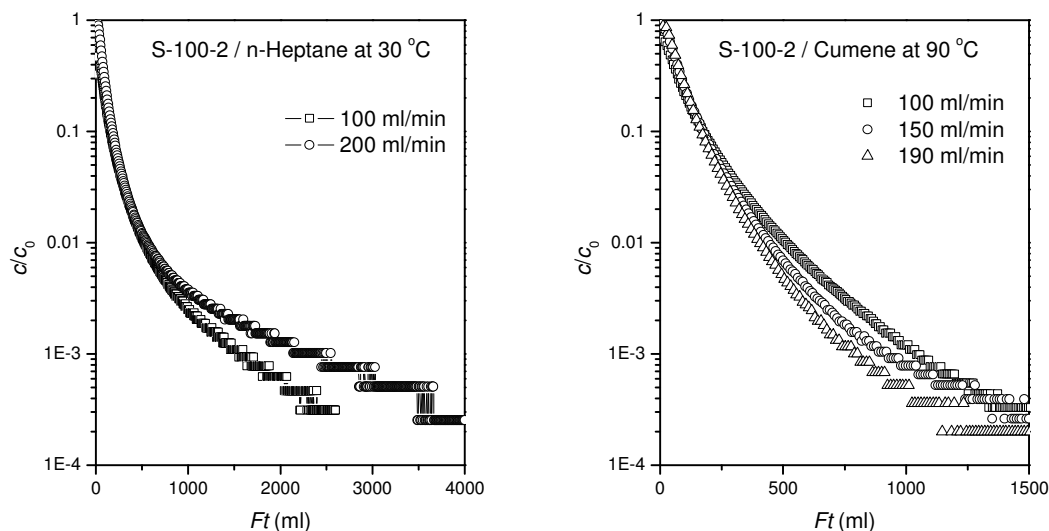
Just like the structural properties reported in the previous chapter, the diffusion results of the different hydrocarbons are strongly varying as a function of the synthesis temperature and time confirming a close relationship of micro- and mesostructure and diffusivity. A remarkable increase in effective diffusivity is observed as a function of increasing synthesis time and temperature caused by a successive enlargement of the porous structure as described in the previous chapter. For all samples except S-45-1,

²Only under assumption of the same Henry constant for all samples

CHAPTER 5. DIFFUSIONAL PROPERTIES

Sample	Sorbate	T (°C)	L	D_{eff}/R^2 (s ⁻¹)	D_{eff} (m ² s ⁻¹)	E_A (kJ/mol)
S-45-1	n-heptane	10	40	$1.58 \cdot 10^{-4}$	$6.34 \cdot 10^{-14}$	6
		30	43	$2.11 \cdot 10^{-4}$	$8.45 \cdot 10^{-14}$	
		50	50	$2.67 \cdot 10^{-4}$	$1.07 \cdot 10^{-13}$	
	cumene	30	59	$1.36 \cdot 10^{-4}$	$5.43 \cdot 10^{-14}$	6
		50	67	$1.59 \cdot 10^{-4}$	$6.34 \cdot 10^{-14}$	
		70	112	$1.79 \cdot 10^{-4}$	$7.15 \cdot 10^{-14}$	
	mesitylene	30	246	$1.51 \cdot 10^{-4}$	$6.04 \cdot 10^{-14}$	8.2
		50	361	$1.84 \cdot 10^{-4}$	$7.37 \cdot 10^{-14}$	
		70	641	$2.21 \cdot 10^{-4}$	$8.83 \cdot 10^{-14}$	
S-60-1 (15 μ m)	n-heptane	10	40	$3.41 \cdot 10^{-4}$	$7.67 \cdot 10^{-14}$	9.6
		30	53	$4.62 \cdot 10^{-4}$	$1.04 \cdot 10^{-13}$	
		50	87	$5.62 \cdot 10^{-4}$	$1.27 \cdot 10^{-13}$	
	cumene	50	18	$1.57 \cdot 10^{-4}$	$3.53 \cdot 10^{-14}$	28.3
		70	29	$2.38 \cdot 10^{-4}$	$5.35 \cdot 10^{-14}$	
		90	50	$5.03 \cdot 10^{-4}$	$1.13 \cdot 10^{-13}$	
	mesitylene	50	27	$1.22 \cdot 10^{-4}$	$2.74 \cdot 10^{-14}$	20.6
		70	41	$1.78 \cdot 10^{-4}$	$4.00 \cdot 10^{-14}$	
		90	81	$2.85 \cdot 10^{-4}$	$6.40 \cdot 10^{-14}$	
S-80-1 (20 μ m)	n-heptane	10	20	$3.26 \cdot 10^{-4}$	$1.30 \cdot 10^{-13}$	13.3
		30	27	$4.79 \cdot 10^{-4}$	$1.92 \cdot 10^{-13}$	
		50	55	$6.55 \cdot 10^{-4}$	$2.62 \cdot 10^{-13}$	
	cumene	50	12	$1.24 \cdot 10^{-4}$	$4.98 \cdot 10^{-14}$	29.7
		70	13	$2.24 \cdot 10^{-4}$	$8.96 \cdot 10^{-14}$	
		90	48	$4.34 \cdot 10^{-4}$	$1.69 \cdot 10^{-13}$	
	mesitylene	50	12	$1.19 \cdot 10^{-4}$	$4.77 \cdot 10^{-14}$	25.8
		70	13	$2.10 \cdot 10^{-4}$	$8.41 \cdot 10^{-14}$	
		90	21	$3.44 \cdot 10^{-4}$	$1.38 \cdot 10^{-13}$	
S-80-5 (23 μ m)	n-heptane	10	25	$3.12 \cdot 10^{-4}$	$1.65 \cdot 10^{-13}$	19.9
		30	41	$4.83 \cdot 10^{-4}$	$2.55 \cdot 10^{-13}$	
		50	80	$8.93 \cdot 10^{-4}$	$4.72 \cdot 10^{-13}$	
	cumene	50	16	$1.75 \cdot 10^{-4}$	$9.26 \cdot 10^{-14}$	39.5
		70	20	$3.96 \cdot 10^{-4}$	$2.09 \cdot 10^{-13}$	
		90	43	$8.86 \cdot 10^{-4}$	$4.68 \cdot 10^{-13}$	
	mesitylene	50	12	$1.71 \cdot 10^{-4}$	$9.07 \cdot 10^{-14}$	34.2
		70	15	$3.66 \cdot 10^{-4}$	$1.94 \cdot 10^{-13}$	
		90	30	$6.97 \cdot 10^{-4}$	$3.69 \cdot 10^{-13}$	
S-100-1 (23 μ m)	n-heptane	10	25	$2.40 \cdot 10^{-4}$	$1.27 \cdot 10^{-13}$	22.2
		30	52	$4.13 \cdot 10^{-4}$	$2.19 \cdot 10^{-13}$	
		50	96	$7.74 \cdot 10^{-4}$	$4.10 \cdot 10^{-13}$	
	cumene	50	15	$1.54 \cdot 10^{-4}$	$8.12 \cdot 10^{-14}$	40.4
		70	20	$3.66 \cdot 10^{-4}$	$1.94 \cdot 10^{-13}$	
		90	59	$8.05 \cdot 10^{-4}$	$4.26 \cdot 10^{-13}$	
	mesitylene	50	17	$1.37 \cdot 10^{-4}$	$7.22 \cdot 10^{-14}$	35.5
		70	26	$2.55 \cdot 10^{-4}$	$1.35 \cdot 10^{-13}$	
		90	34	$5.89 \cdot 10^{-4}$	$3.11 \cdot 10^{-13}$	
S-100-2 (24 μ m)	n-heptane	10	14	$4.52 \cdot 10^{-4}$	$2.60 \cdot 10^{-13}$	24.7
		30	23	$7.46 \cdot 10^{-4}$	$4.29 \cdot 10^{-13}$	
		50	53	$1.67 \cdot 10^{-3}$	$9.62 \cdot 10^{-13}$	
	cumene	50	20	$1.92 \cdot 10^{-4}$	$1.11 \cdot 10^{-13}$	47.9
		70	28	$4.61 \cdot 10^{-4}$	$2.65 \cdot 10^{-13}$	
		90	36	$1.38 \cdot 10^{-3}$	$7.96 \cdot 10^{-13}$	
	mesitylene	50	20	$1.58 \cdot 10^{-4}$	$9.07 \cdot 10^{-14}$	41.8
		70	24	$3.66 \cdot 10^{-4}$	$2.11 \cdot 10^{-13}$	
		90	36	$8.75 \cdot 10^{-4}$	$5.04 \cdot 10^{-13}$	

Table 5.1.: Diffusivity data of n-heptane, cumene and mesitylene for SBA-16 samples.

Figure 5.1.: Ft -plots for S-100-2.

the effective diffusion of n-heptane is the fastest followed by cumene and mesitylene respectively, as expected if the kinetic diameter of the molecules is the limiting factor for diffusion. n-heptane has a kinetic diameter of 0.43 nm, cumene has a kinetic diameter of 0.67 nm and mesitylene of 0.87 nm [95]. For the SBA-16 sample S-45-1 synthesized at low temperature, with thick and highly microporous walls, n-heptane shows a typical diffusion for a micro- or mesoporous material (see Figures 5.3a). It enters easily (kinetically fast) the porous structure. The diffusion mechanism is mostly intracrystalline and Knudsen diffusion. In contrast the adsorption kinetics of cumene and mesitylene are very slow, the equilibrium is very difficult to reach in a short period of time. The diffusion is a combination of a fast surface barrier [87] at short times and a slow intracrystalline diffusion mechanism at longer times. Interestingly the diffusion of mesitylene is faster than the one of cumene. Both molecules seem to be in the size of the porous structure. In this material the primary mesopores are only interconnected by micropores. The larger interconnections of the main cavities typical for the SBA-16 structure seem to be undeveloped and thus also being in the size of the intrawall microporosity. This size is the limiting pore size for mesitylene and cumene, thereby it is more difficult for mesitylene to enter the pore structure. As a conclusion the micropore diameter in S-45-1 is larger than the kinetic size of n-heptane but in the range of the kinetic sizes of cumene or mesitylene confirming the calculations of the intrawall micropore diameter in the previous chapter.

Increasing the synthesis temperature from 45 °C to 60 °C for sample S-60-1 directly yields in a more developed structure. The interconnections between the primary mesopores or the so called pore entrance sizes are now large enough for cumene and mesitylene to enter the porous structure kinetically fast. The diffusion mechanism is not longer surface barrier. Also the great change in activation energy for cumene and mesitylene is an indication of a complete different diffusion mechanism. In contrast, the activation energy of n-heptane is practically the same than the one for S-45-1, the dominant part of

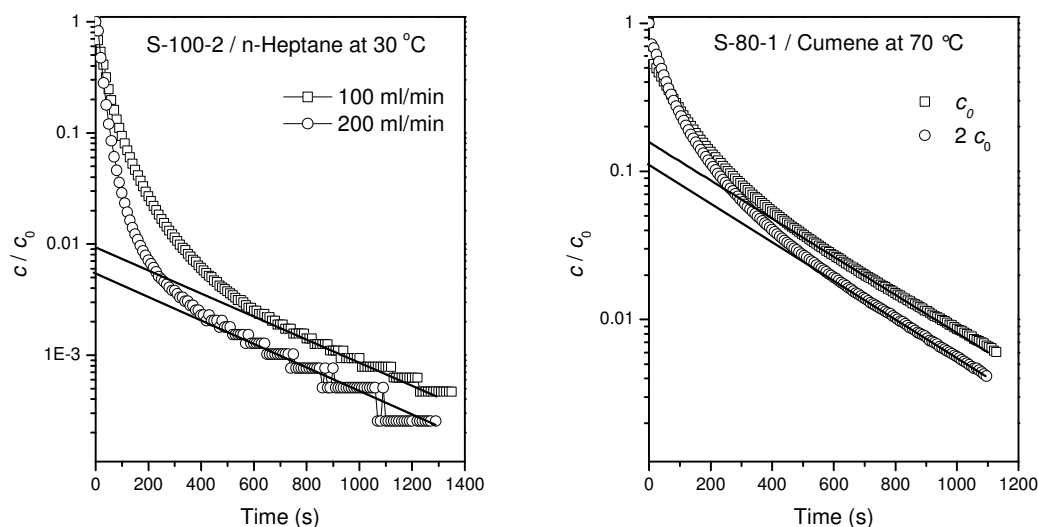


Figure 5.2.: Experimental ZLC curves at varying flow rate (A) and varying sorbate concentration (B).

diffusion still takes place in the micropores. Due to the change in activation energy it might be that the dominant part of diffusion of cumene and mesitylene now takes place through the open pore structure and not through the intrawall micropores. Thereby the change in activation energy is less pronounced for mesitylene (see Figure 5.5), thus some microporous limitations are still occurring. However the easiest way to pass from one mesopore to another are for both molecules the larger interconnections between the primary mesopores. It is obvious that each time a molecule passes a mesopore it is attracted by the pore wall and is thus sliding on the microporous walls from one cavity to another. The diffusion mechanism could be dominated by a surface or so called slip-type diffusion [96, 97]. This type of diffusion is strongly temperature dependent and thus could explain the high activations energies observed for all hydrocarbons for the samples synthesized at 80 °C to 100 °C.

For these samples the effective diffusion increases in a linear way as a function of the mesoporosity as plotted in Figure 5.4. The activation energy is also increasing linear as a function of the mesoporosity (Figure 5.5). This suggests the same diffusion mechanism for all these samples. In the SBA-15 series [25, 98] the activation energy decreased as a function of the mesoporosity as expected if Knudsen and intracrystalline diffusion are the dominating mechanisms. However, this phenomenon can not be explained by a simple diffusion mechanism, it has to be related to the structure of SBA-16 materials which can be represented by a triply periodic minimal surface of I-WP (body centered, wrapped package) as stated in the previous chapter. Also the pore blocking and pore network effects which are directly related to the I-WP structure have to be taken into consideration. Assuming a surface diffusion as dominant diffusion mechanism in such a specific structure, it is obvious that in a material with large mesopore diameters like S-100-2 of about 13.3 nm and still relatively small pore entrance sizes of under 4 nm (probably around 2-3

CHAPTER 5. DIFFUSIONAL PROPERTIES

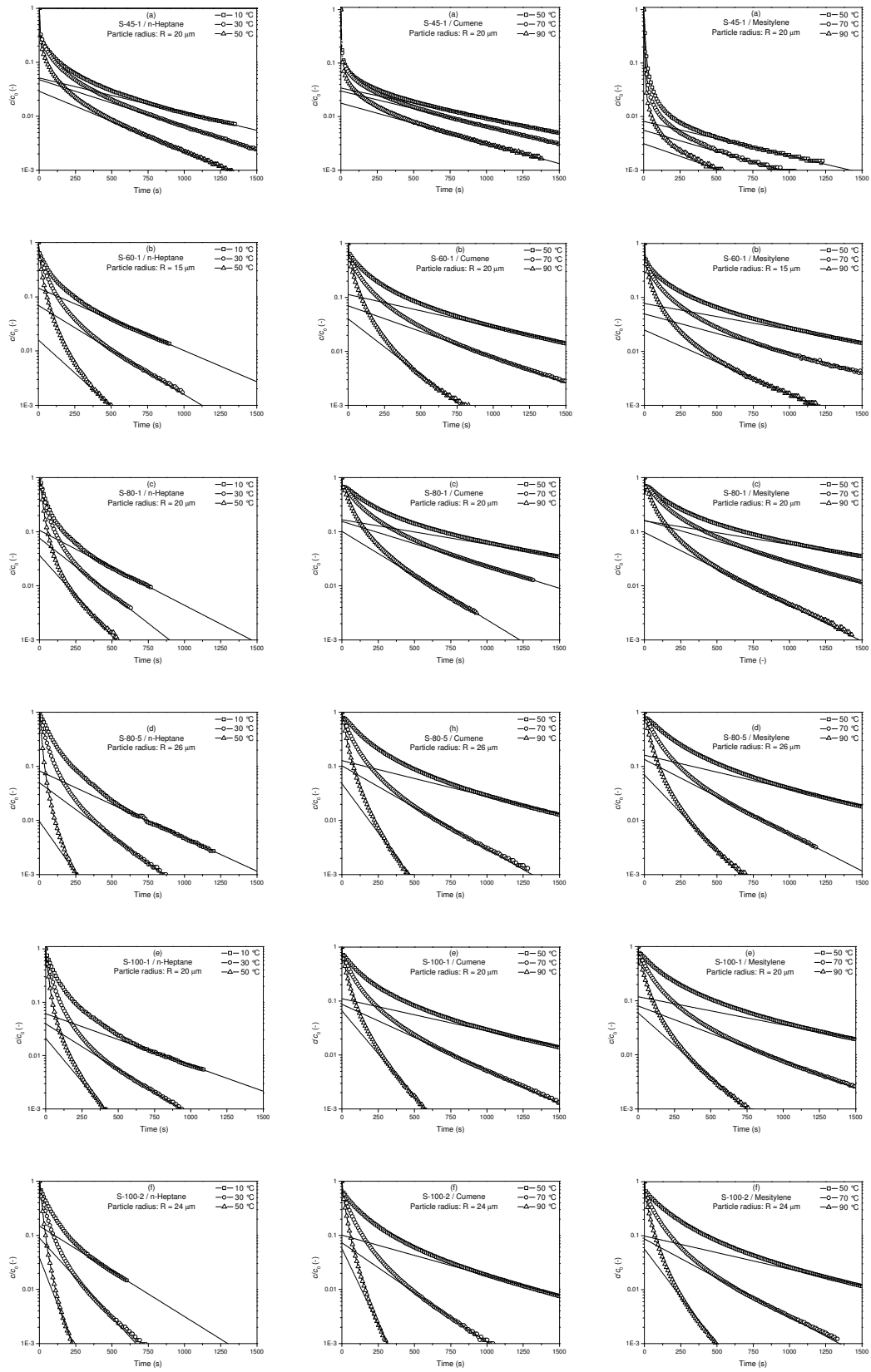


Figure 5.3.: Experimental ZLC curves and long time solution of SBA-16 samples at flow rate of 100 ml/min: (a) S-45-1; (b) S-60-1; (c) S-80-1; (d) S-80-5; (e) S-100-1; (f) S-100-2.

CHAPTER 5. DIFFUSIONAL PROPERTIES

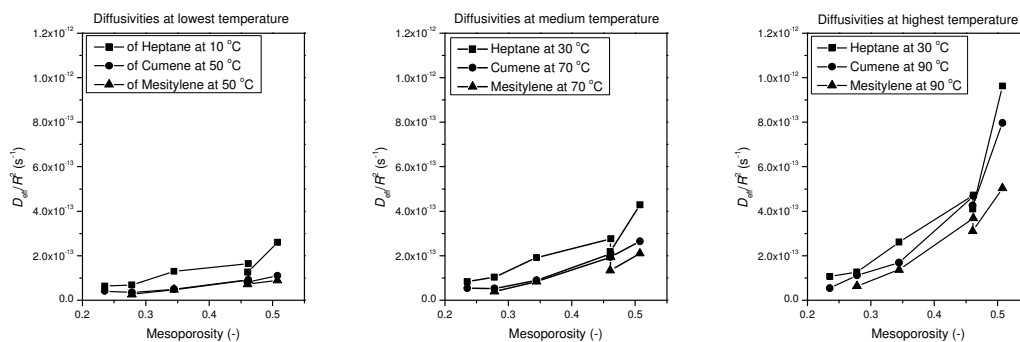


Figure 5.4.: Diffusivities at different temperatures.

nm [99]) it is difficult for the hydrocarbons to diffuse from one mesopore to another if there is a lack of kinetic energy. In a material with smaller mesopores or larger pore entrance sizes the time of flight or a jump of a molecule before being attracted to a wall is probably longer, leading to a greater mean square displacements from one jump to another. SBA-15 materials with cylindrical mesopores can be considered as a boundary case with pore entrances as large as the pore itself. In this case a longer molecule jump signifies a longer gas phase diffusion which is only weakly temperature dependent. In contrast in a pore blocked SBA-16 material with network effects the number of jumps before passing from one mesopore to another is higher and the time of a jump is probably shorter leading to a more dominant surface diffusion than in SBA-15 materials.

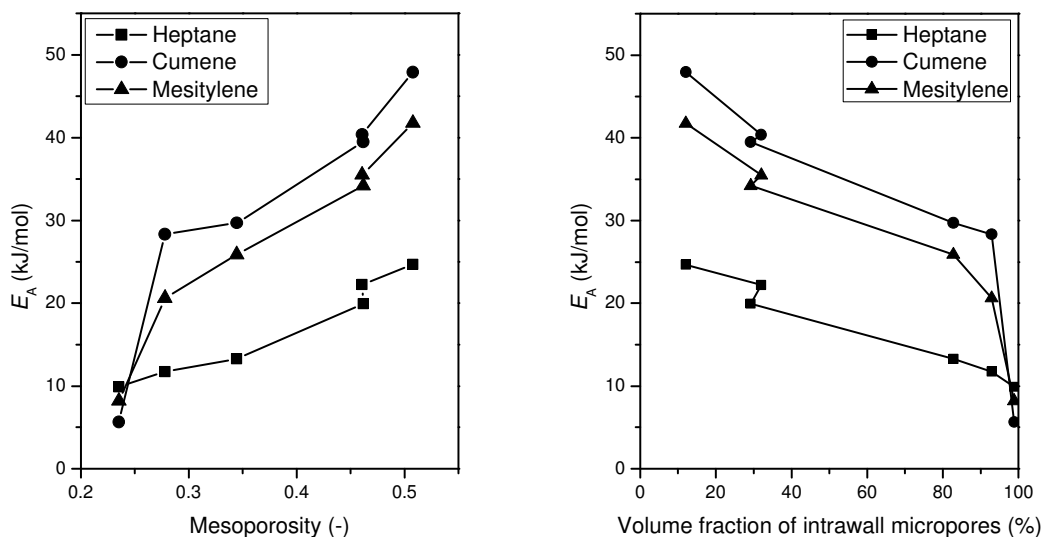


Figure 5.5.: Activations energies of different samples.

Another very interesting result is related to the order of activation energies for the three hydrocarbons which is different than the one observed for the same hydrocarbons for SBA-15 materials [25, 98]. For the SBA-15 materials the activation energy of mesitylene was higher than the one of cumene. For the SBA-16 series investigated in this study, the

diffusion of mesitylene in all samples except S-45-1 is less activated than the diffusion of cumene. This behavior also has to be related to the surface type diffusion mechanism and the particular structure of SBA-16 materials. The higher polarity of cumene in contrast to mesitylene could lead to a stronger interaction with the silicate walls and respectively to shorter surface jumps and displacements. Also the asymmetry of cumene and the greater moment of inertia compared to mesitylene could require additional kinetic energy for a successful surface displacement or jump. The diffusion of n-heptane is as expected the least activated, confirming the assumption of a more dominant Knudsen diffusion. Anyhow, the increasing activation energy for n-heptane for the samples with larger mesopores is an indication, that the diffusion takes place dominantly in the primary mesopores in contrast to a diffusion through the intrawall pores for S-45-1 and S-60-1. The differences in temperature dependence of diffusion between SBA-15 and SBA-16 are visualized by Arrhenius plots in Figures 5.6 and 5.7.

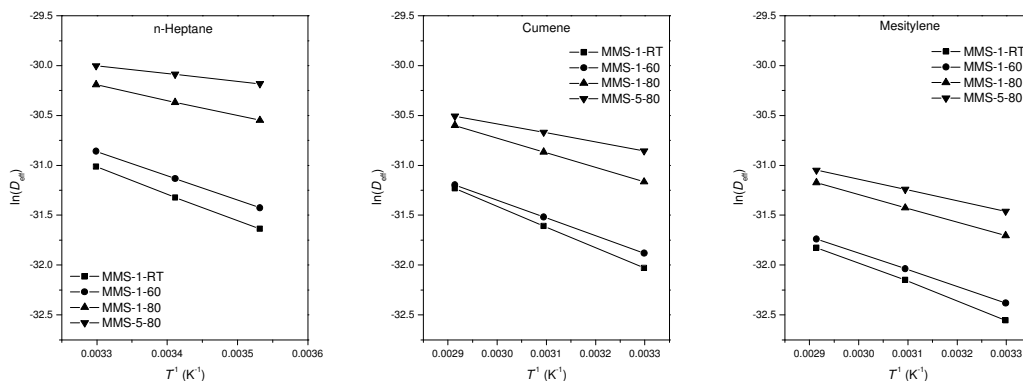


Figure 5.6.: Arrhenius plots of SBA-15 samples, from Hoang et al. [25, 98].

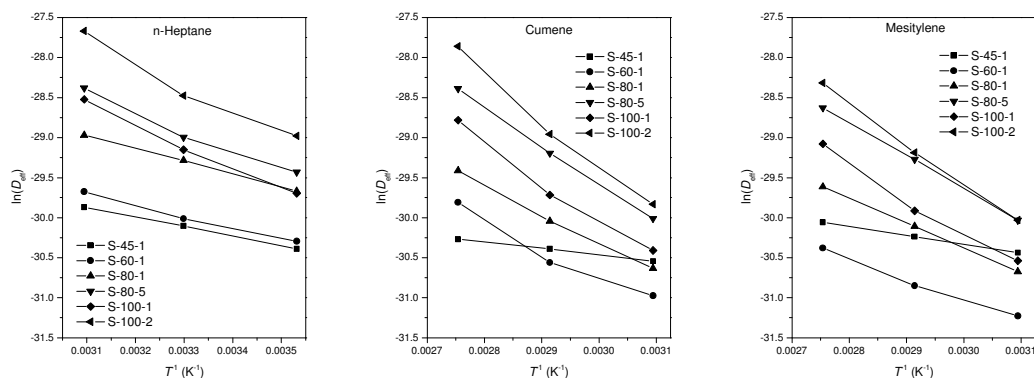


Figure 5.7.: Arrhenius plots of SBA-16 samples

The two materials S-80-5 and S-100-1 synthesized under different conditions have very similar adsorption and structural properties. The diffusion is also very similar, confirming the strong relationship of micro- and mesostructure and diffusivity. It also shows, that similar materials can be obtained in a long time synthesis at lower temperature or in a short time synthesis at higher temperature.

To compare the effective diffusion results with other studies the particle sizes of the SBA-16 samples have to be obtained. As stated before only the biggest particles are relevant for the long-time analysis. The obtained sizes and the effective diffusion are shown in Table 5.1. The effective diffusion is for all samples faster than the one in SBA-15 materials. This can be certainly related to the 3-D pore structure of SBA-16 in contrast to the only 1-D mesopore diffusion and the more inhibited 3-D intrawall diffusion of SBA-15.

5.4. Conclusions

The diffusion properties of probe molecules, i.e. n-heptane, cumene and mesitylene in SBA-16 materials with a 3-D cubic mesoporous structure were investigated using the ZLC technique. The strong relationship of micro- and mesostructure and diffusivity already observed for SBA-15 materials could be confirmed. For a complete description of the diffusional properties micro- and mesoporous limitations have to be taken into account. As a result of the 3-D mesoporous structure the effective diffusivities are very high in contrast to the diffusion in SBA-15 or microporous zeolites. The diffusivities are highly temperature dependent leading to activation energies nearly as high as in microporous materials. However the high activation energies are not related to microporous limitations. The particular structure, which consists in a pore blocked structure with network effects, in combination with a highly temperature dependent surface diffusion mechanism leads to such a temperature dependency. This result is very important for the use of SBA-16 as a catalyst. Only at higher temperatures the SBA-16 materials will present a high activity. The systematically highest activation energy for cumene observed in this study can also be related to the particular SBA-16 structure and to the diffusion mechanism. This will be further investigated by analyzing the adsorption properties of SBA-16 in the next chapter.

6. Adsorption of hydrocarbons

6.1. Results and Discussion

The sorption isotherms of n-heptane and toluene were obtained for three SBA-16 samples with different structural properties. These are the samples S-45-1, S-80-5 and S-100-2. For S-80-5 additionally to the adsorption isotherm, also the desorption isotherm was recorded for 25 °C and 30 °C. Figure 6.1. summarizes these adsorption and desorption isotherms, expressed as a function of the partial pressure of the sorbate in Pascal and Torr. The unit Torr was chosen additionally for an easy comparison with the sorption results of prior works, such as the SBA-15 series, where the partial pressure is expressed in Torr. The amounts adsorbed are expressed in millimol and volumes of liquid sorbate. For some of the samples the measurements of the the low pressure region are rather bad. The analysis, especially of the low pressure region, has to be done with care and is sometimes not possible.

As expected all the isotherms are just like the nitrogen physisorption isotherms of type IV according to the IUPAC classification. The desorption isotherm, only recorded for sample S-80-5, shows the same hysteresis loop of type H2 as for the nitrogen measurements at 77 K. The hysteresis loop is well pronounced and very steep, thus the same spinodal desorption mechanism applies for bulkier sorbates than nitrogen and at higher temperatures.

Sample	nitrogen	n-heptane	toluene
S-45-1	0.234	0.148	0.144
S-80-5	0.678	0.495	0.498
S-100-2	0.773	0.553	0.562

Table 6.1.: Total pore volume (V_t , cm³/g) calculated from the adsorption isotherms of different sorbates.

The n-heptane and toluene uptake at low pressures decreases as a function of the microporosity of the samples (S-45-1 > S-80-5 > S-100-2). For the highly microporous SBA-16 sample S-45-1 the uptake is particularly pronounced. Thereby toluene is stronger adsorbed at low pressures than n-heptane (Figure 6.1 insets and Figure 6.2). Similar results were recently reported by Vinh-Thang et al. [88] for SBA-15 materials. The pressure of capillary condensation increases from about 0.3 p/p_0 to nearly 0.6 p/p_0 ³, due

³for nitrogen: 0.5 p/p_0 to nearly 0.8 p/p_0

CHAPTER 6. ADSORPTION OF HYDROCARBONS

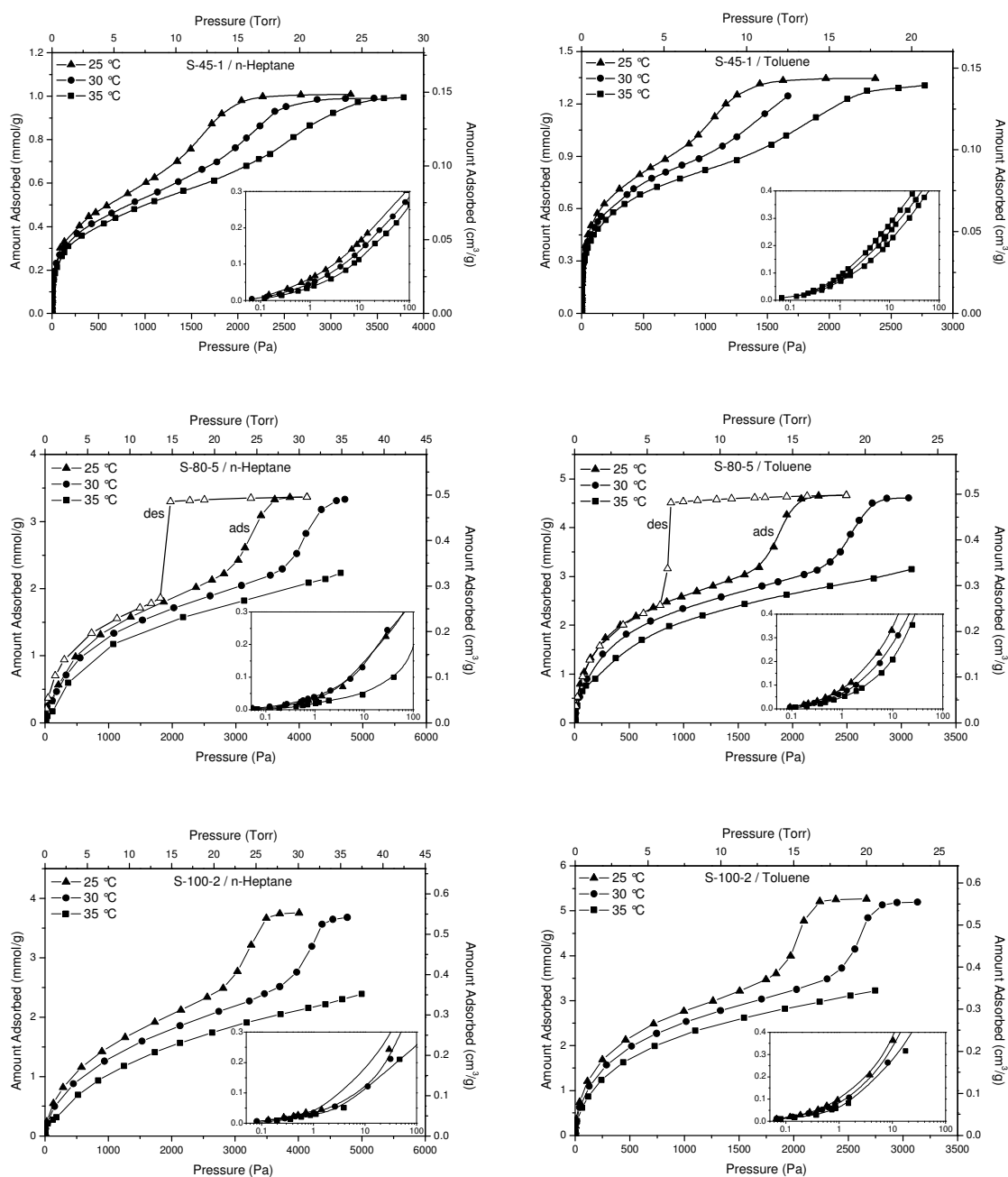


Figure 6.1.: Sorption isotherms of n-heptane and toluene on selected SBA-16 samples at 25 °C, 30 °C and 35 °C respectively. For sample S-80-5 the desorption isotherm at 25 °C is also shown. The low pressure region of the isotherms is plotted on a semi-logarithmic scale in the inset figures. The amounts adsorbed are expressed in millimol and volumes of liquid sorbate.

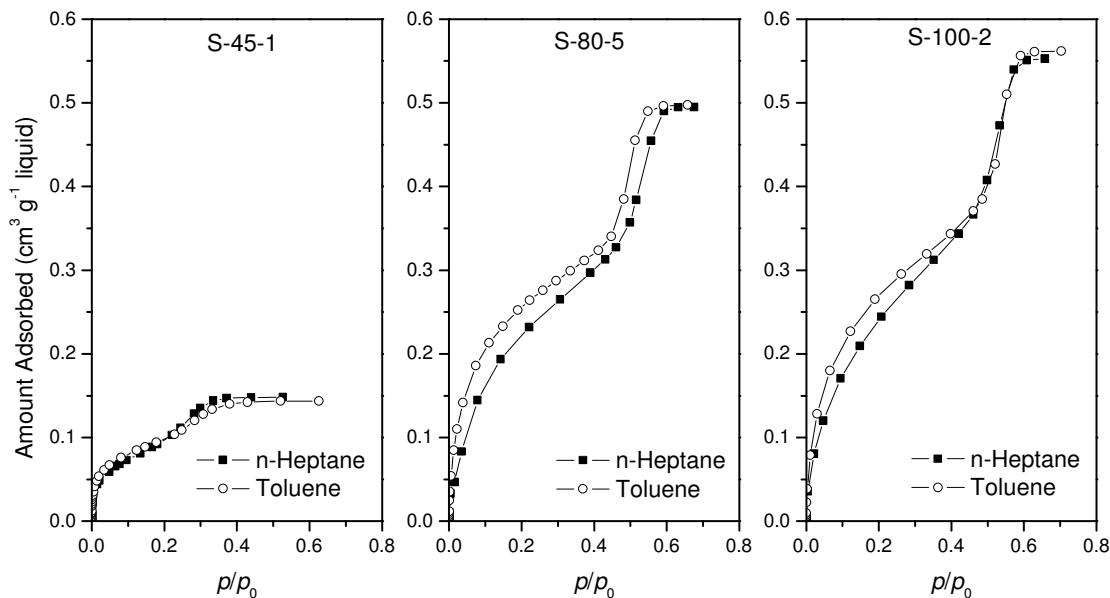


Figure 6.2.: Sorption isotherms of n-heptane and toluene on selected SBA-16 samples at 25 °C. The amounts adsorbed are expressed in volumes of liquid sorbate.

to the increase of the mesopores diameter for the samples synthesized at longer aging times or higher aging temperatures ($S-45-1 < S-80-5 < S-100-2$).

In Table 6.1 the values of the total pore volume estimated from the high pressure region of the isotherms at 25 °C and the pore volume for nitrogen adsorption at 77 K can be found. As expected according to Gurvitsch rule [100] and also observed by Vinh-Thang et al. [88] for SBA-15 materials, the maximum values of the pore volumes for the two hydrocarbons are almost identical. The values obtained from the nitrogen physisorption are in contrast about 20 to 30 % higher. van Bavel et al. [101] explained this effect by the partial filling of the micropores of SBA-15 materials by the bulkier hydrocarbons. As discussed by Vinh-Thang et al. [88] the contribution of the microporosity to the differences in the density of adsorbed and liquid hydrocarbons can not play a major role, because the differences of the total pore volume estimated by nitrogen and hydrocarbon adsorption are larger than the micropore volume of the samples. Also for the SBA-16 series, the micropore volume is not large enough to explain the difference. On the basis of the analysis of the heat of adsorption, Vinh-Thang et al. [88] proposed an other explanation for this effect. Lateral sorbate-sorbate interactions, in which the first layers of adsorbed molecules are successively preventing the following layers to interact with the pore walls, could lead to less strongly adsorbed molecules. The density of the adsorbed phase should then be lower than that of the free liquid phase. This, probably together with the 'micropore effect' [101], could explain why the total pore volume estimated by hydrocarbon sorption is found to be significantly lower than the one obtained by nitrogen physisorption.

Heat of adsorption

In Figure 6.3 the isosteric heat of adsorption is plotted against the surface coverage for the adsorption of n-heptane and toluene. For toluene the isosteric heat of adsorption at very low coverage is very low, sometimes lower than the heat of vaporisation of toluene. This could be related somehow to the structure of the materials, but certainly experimental error affect the results. For a proper analysis, further experiments have to be carried out. Also at high surface coverage, but at partial pressures still under the capillary condensation pressure, the results for toluene are in a strange order. For S-80- 5, the isosteric heat of adsorption is the highest.

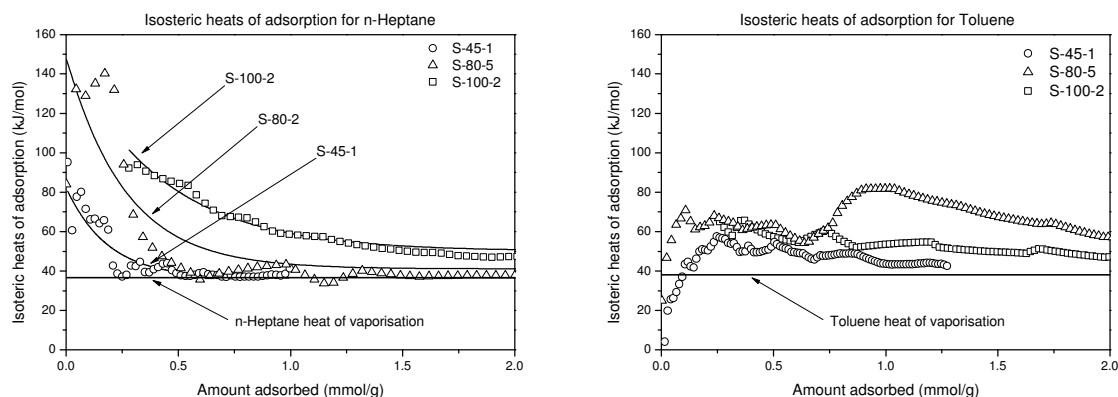


Figure 6.3.: Dependence of isosteric heat of adsorption with surface coverage for the adsorption of n-heptane and toluene on SBA-16.

In contrast the results for n-heptane seem to be more consistent, especially at high coverage. The fitting curves in Figure 6.3 represent the exponential decrease of the heat of adsorption with the surface coverage. This initial sharp decrease was observed for many micro- and mesoporous systems, these are for instance MFI zeolites [74, 77, 81] or MCM-41 materials [102]. Also recently for SBA-15 samples [88, 103, 104] this effect could be observed. This decrease has often been ascribed to the heterogeneity of adsorption sites [103, 104]. Another explanation for the exponential decrease are the lateral sorbate-sorbate interactions, which were already mentioned in the previous section.

Especially at high coverage, but also at low coverage, the isosteric heat of adsorption for n-heptane is in the following order: S-100-2 > S-80-5 > S-45-1. Vinh-Thang et al. observed for the sorption of n-heptane on SBA-15 samples the inverse order, in regard of the structural properties of the samples i.e. micro- and mesoporosity: MMS-5-80 > MMS-1-80 > MMS-1-60 > MMS-1-RT. The observed order for n-heptane is a confirmation of the calculated heat of adsorption from the ZLC measurements and could be an explanation to the inverse relationship of the effective diffusivity as discussed in chapter 5.

All the discussions concerning the heat of adsorption have to be taken with care. Most of the measurements seem to be erroneous at low pressures. Also there is not

CHAPTER 6. ADSORPTION OF HYDROCARBONS

enough reliable experimental data available for an accurate or even statistical analysis. Anyhow, some interesting effects could be distinguished, which surely require further investigation in the future.

7. Conclusions and perspectives

For the first time, SBA-16 materials containing both micro and mesopores with a mesostructure, where pore blocking and network effects play a major role, were synthesized and characterized by diffusion and sorption experiments.

Using a new kind of synthesis route under low acid concentration and with butanol as cosurfactant agent, it was possible to obtain a high-quality SBA-16 series by variation of the time or temperature of the aging or hydrothermal treatment step. Thereby the intrawall porosity was systematically controlled in order to get materials with a high fraction of intrawall micropores and thick walls up to materials with few micropores, thin walls and large primary mesopores. For all materials the pore entrance size remained under 4 nm.

Using the ZLC method to measure the intracrystalline diffusivities of n-heptane, cumene and mesitylene, interesting effects could be observed which are certainly related to the specific structure of SBA-16. Further investigation should be taken into consideration especially with respect to the mesostructure of materials showing pore blocking and network effects, as for instance KIT-5 materials. Also higher hydrothermal treatment temperatures would cause an enlargement of the pore entrances, which could have very interesting properties, with less pronounced pore blocking effects. Furthermore, diffusional studies on MCM-48 and KIT-6 materials, showing both a rather near equilibrium desorption just like MCM-41 or SBA-15, would be very interesting. The sorption experiments, which are directly related to the diffusional properties, should be repeated in an in-depth analysis, to complete and to explain in a more quantitative way the observed effects.

A. Derivation of model equations

A.1. Differential ZLC-Model

Derivation of the mathematical ZLC model, from Brandani et al. [74].

As stated in the experimental section the two governing equations are the fluid-phase and the solid-phase mass balance in radial coordinates, without negligence of the fluid-phase hold-up:

$$V_s \frac{d\bar{q}}{dt} + V_f \frac{dc}{dt} + F \cdot c(t) = 0 \quad (\text{A.1})$$

$$\frac{\partial q}{\partial t} = D \cdot \left(\frac{\partial^2 q}{\partial r^2} + \frac{2}{r} \frac{\partial q}{\partial r} \right) \quad (\text{A.2})$$

where \bar{q} is the value of q averaged over the particle.

The initial conditions of the system are:

$$q(r, 0) = q_0 K_H c_0; \quad c(0) = c_0 \quad (\text{A.3})$$

and the boundary condition:

$$\left(\frac{\partial q}{\partial r} \right)_{r=0} = 0 \quad (\text{A.4})$$

Equation A.1 can be considered as a boundary condition on the solid-phase mass balance:

$$\frac{4}{3} \pi R^3 \frac{d\bar{q}}{dt} = 4 \pi R^2 D \left(\frac{\partial q}{\partial r} \right)_{r=R} \quad (\text{A.5})$$

with equilibrium at the surface:

$$q(R, t) = K_H c(t) \quad (\text{A.6})$$

The fluid-phase mass balance A.1 can then be written as:

$$\frac{3}{R} D V_s \frac{\partial q}{\partial r} + \frac{V_f}{K_H} \frac{\partial q}{\partial t} + \frac{F}{K_H} q \Big|_{r=R} = 0 \quad (\text{A.7})$$

Introducing the change of variable ($\zeta = rq$), equation A.2 reduces to:

$$\frac{\partial \zeta}{\partial t} = D \frac{\partial^2 \zeta}{\partial r^2} \quad (\text{A.8})$$

Since $q(r, t)$ is always finite the boundary condition in equation A.4, can be rewritten as:

$$\zeta(0, t) = 0 \quad (\text{A.9})$$

Equation A.8 can be solved through separation of variables:

$$\zeta(r, t) = Q(r) \cdot T(t) \quad (\text{A.10})$$

$$Q \frac{dT}{dt} = DT \frac{d^2 Q}{dr^2} \quad (\text{A.11})$$

or

$$\frac{1}{DT} \frac{dT}{dt} = \frac{1}{Q} \frac{d^2 Q}{dr^2} = -\lambda^2 \quad (\text{A.12})$$

where λ is a constant. These differential equations are separable and give the following solution:

$$T = C \exp(-\lambda^2 Dt); \quad Q = A \sin(\lambda r) + B \cos(\lambda r) \quad (\text{A.13})$$

where λ must be real (ζ is always finite). Furthermore, from equation (A.9) it follows that B must be zero. The general solution is given by:

$$q = \frac{a}{r} \sin(\lambda r) \cdot \exp(-D\lambda^2 t) \quad (\text{A.14})$$

where $a = AC$.

Substituting in the fluid-phase mass balance (A.7):

$$\frac{3DV_s}{R} \left(\frac{\lambda}{R} \cos(\lambda R) - \frac{1}{R^2} \sin(\lambda R) \right) - \frac{D\lambda^2 V_f}{K_H R} \sin(\lambda R) + \frac{F}{K_H R} \sin(\lambda R) = 0 \quad (\text{A.15})$$

which give as the characteristic equation:

$$\beta_n \cot \beta_n + L - 1 - \gamma \beta_n^2 = 0 \quad (\text{A.16})$$

with

$$L = \frac{1}{3} \frac{F}{K_H V_s} \frac{R^2}{D}; \quad \gamma = \frac{1}{3} \frac{V_f}{K_H V_s} \quad \beta = \lambda R \quad (\text{A.17})$$

The general solution is therefore given by:

$$q(r, t) = \sum \frac{a_n}{r} \sin\left(\beta_n \frac{r}{R}\right) \cdot \exp\left(-\beta_n^2 \frac{D}{R^2} t\right) \quad (\text{A.18})$$

And for the initial condition:

$$q(r, 0) = q_0 = \sum \frac{a_n}{r} \sin\left(\beta_n \frac{r}{R}\right) \quad (\text{A.19})$$

To evaluate a_n , we have to consider the following integral:

$$\int_0^R \sin\left(\beta_n \frac{r}{R}\right) \sin\left(\beta_m \frac{r}{R}\right) dr \quad (\text{A.20})$$

After integrating twice by parts and taking into account equation (A.16) and (A.19) we get for a_n (see Brandani et al. [74]):

$$a_n = \frac{\int_0^R r q_0 \sin(\beta_n r/R) dr + \gamma R^2 q_0 \sin \beta_n}{\int_0^R \sin^2(\beta_n r/R) dr + \gamma R \sin^2 \beta_n} \quad (\text{A.21})$$

taking into account equation A.16:

$$\frac{a_n}{q_0} = \frac{2R}{\sin \beta_n} \cdot \frac{L}{\beta_n^2 + (1 - L + \gamma\beta_n^2)^2 + L - 1 + \gamma\beta_n^2} \quad (\text{A.22})$$

The solution of the problem is therefore given by:

$$\frac{q(r, t)}{q_0} = \frac{R}{r} \sum \frac{2L}{\beta_n^2 + (1 - L + \gamma\beta_n^2)^2 + L - 1 + \gamma\beta_n^2} \cdot \frac{\sin(\beta_n r / R)}{\sin \beta_n} \cdot \exp\left(-\beta_n^2 \frac{D}{R^2} t\right) \quad (\text{A.23})$$

for $r = R$ and under assumption of linearity of the system¹, we get the desorption curve:

$$\frac{c(t)}{c_0} = \sum \frac{2L}{\beta_n^2 + (1 - L + \gamma\beta_n^2)^2 + L - 1 + \gamma\beta_n^2} \cdot \exp\left(-\beta_n^2 \frac{D}{R^2} t\right) \quad (\text{A.24})$$

where β_n are the positive roots of equation A.16. Under negligence of the fluid-phase hold-up ($\gamma = 0$), the solution reduces to:

$$\frac{c(t)}{c_0} = \sum \frac{2L}{\beta_n^2 + L(L - 1)} \cdot \exp\left(-\beta_n^2 \frac{D}{R^2} t\right) \quad (\text{A.25})$$

which is the final form of the ZLC model used in this thesis (see equation (3.22)).

¹The adsorbed-phase concentration q can be described as a linear function of the fluid-phase concentration c .

B. Source codes

B.1. Matlab source codes

All the listings in this section are only source snippets showing the relevant part of the computations. Missing parts are represented by: '...'.

Listing B.1: Optimized Brunnauer-Emmett-Teller analysis

```
1 function [V_t_STP, V_t, V_BET, S_BET, a, b, c, q_ad] = f_bet(data, p_min, p_max)
2
3 % declaration of variables:
4
5 [...]
6
7 % find indexes 'i_min' and 'i_max' corresponding to the minimum and maximum
8 % pressure in adsorption data:
9
10 [...]
11
12 % optimize BET parameters in given range:
13 for i=i_min:i_max-1
14     cnt++;
15     p_red = data([i_min:i+1],1);
16     V = data([i_min:i+1],2);
17
18     y = p_red ./ (V .* (1 - p_red));
19
20     % BET linear fit:
21     [P, YF] = polyfit(p_red, y, 1);
22
23     V_array(cnt,1) = i-i_min;
24     V_array(cnt,2) = p_red(i-i_min+1);
25     V_array(cnt,3) = P(1);
26     V_array(cnt,4) = P(2);
27     V_array(cnt,5) = 1 ./ (P(1) + P(2)); % to maximize
28 end
29
30 [mx, mix] = max(V_array(:,5));
31
32 % optimized parameters:
33 a(1) = V_array(mix,3);
34 b(1) = V_array(mix,4);
35
36 % classical BET parameters:
37 a(2) = V_array(end,3);
38 b(2) = V_array(end,4);
39
```

CHAPTER B. APPENDIX B: SOURCE CODES

```

40 % computation of BET values:
41 V_BET = 1 ./ (a + b); % normalized (ml/g)
42 S_BET = 4.37 .* V_BET; % Boer 1963
43 c = a ./ b + 1;
44 q_ad = R .* T .* log(c); % molar net heat of adsorption
45
46 end

```

Listing B.2: PSD calculation with modified BJH method

```

1 function [x PSD dV] = f_psd(data, geom_val)
2
3 % declaration of variables:
4
5 [...]
6
7 % thickness either by analytical equation or by alphas method:
8 t_Harkins = 0.1 .* (60.65 ./ (0.03071 - log10(p))).^(0.3968);
9 t_alphas = alpha_s_interpol .* 0.722; % see Kruk, Jaroniec
10
11 [...]
12
13 % computation of the radius (nm) using the modified Kelvin equation. M. Jaroniec and M. Kruk (1997):
14 for i=1:N
15     r_BJH_Kelvin03(i) = -1 .* geom_val .* gamma .* V_L ./ (R .* T .* log(p(i))) .* 10^(9) + 0.3;
16     r_BJH_mod(i) = -1 .* geom_val .* gamma .* V_L ./ (R .* T .* log(p(i))) .* 10^(9)
17         + t_Harkins(i) + 0.3;
18     r_BJH_mod_as(i) = -1 .* geom_val .* gamma .* V_L ./ (R .* T .* log(p(i))) .* 10^(9)
19         + t_alphas(i) .* 0.722 + 0.3;
20 end
21
22 for i=1:N-1
23     % mean and differential values for BJH-equation
24     r_k_mean(i) = 0.5 .* abs(r_BJH_Kelvin03(i+1) + r_BJH_Kelvin03(i));
25     r_p_mean(i) = 0.5 .* abs(r_BJH_mod(i+1) + r_BJH_mod(i));
26     r_p_mean_as(i) = 0.5 .* abs(r_BJH_mod_as(i+1) + r_BJH_mod_as(i));
27
28     % Original equation without ABS!
29     Dr(i) = abs(r_BJH_mod(i+1) - r_BJH_mod(i));
30     Dt(i) = abs(t_Harkins(i+1) - t_Harkins(i));
31     Dr_as(i) = abs(r_BJH_mod_as(i+1) - r_BJH_mod_as(i));
32     Dt_as(i) = abs(t_alphas(i+1) - t_alphas(i));
33     DV(i) = abs(V(i+1) - V(i));
34 end
35
36 [...]
37
38 % recursive BJH-calculation beginning from maximal pressure at N:
39 for i=1:N-1
40     for j=1:i
41         S += r_p_mean(N-j).^2 ./ ((r_k_mean(N-j) - Dt(N-j)).^2) .* Dt(N-j) .* 2 .* Vp(N-j) ./ r_p_mean(N-j);
42     end
43
44     Ra = r_p_mean(N-i).^2 ./ ((r_k_mean(N-i) + Dt(N-i)).^2);
45     Vp(N-i) = Ra .* abs((DV(N-i) - Dt(N-i) .* sum(S)));
46 end

```

CHAPTER B. APPENDIX B: SOURCE CODES

```

47
48 diameter = 2 .* r_BJH_mod([1:N-1]);
49 dV(1,:) = Vp([1:N-1]);
50 PSD(1,:) = Vp([1:N-1]) ./ (2 .* Dr);
51
52 % 2 pass polynomial smoothing:
53 dV(2,:) = poly_smooth(dV(1,:)', 17, 2, 2);
54 PSD(2,:) = poly_smooth(PSD(1,:)', 17, 2, 2);
55
56 end

```

Listing B.3: ZLC long-time solution

```

1 function [Dr2, L, beta, variance, ysmooth, linfit, ylinfit] = f_ZLC_longtime(t, C, imin, imax, tolerance, dim, gfx)
2 % Zero Length Column, Long Time Solution
3 %
4 % Requires: f_poly_smooth.m
5 %
6 % [Dr2 L beta variance ysmooth linfit ylinfit]
7 % = f_ZLC_longtime(t, C, imin, imax, tolerance, dim, gfx)
8 %
9 % Input:
10 % t: time vector
11 % C: normalized concentration vector of long time region
12 % imin:
13 % imax:
14 % tolerance: accuracy of root (beta) search, default = 1e-4
15 % dim: 1: 1D-Model, 3: 3D-Model (default)
16 % gfx: graphic output, default=1
17 %
18 % Output:
19 % Dr2:
20 % L: error value
21 % beta: root
22 % ysmooth: vector of smoothed concentration
23 % variance: variance of fit
24 % linfit: vector of linear fit
25 % ylinfit: [slope intercept] of linear fit
26
27
28 % check the input:
29 [...]
30
31 % 2 pass, poly-smooth of dataset:
32 C_smooth = f_poly_smooth(C, 17, 2, 2);
33
34 % do a linear fit:
35 lnC = log(C_smooth);
36 p = polyfit(t([imin:imax]), lnC([imin:imax]), 1);
37 intercept_fit = p(2);
38 slope_fit = p(1);
39 variance = sum((lnC([imin:imax]) - (intercept_fit + slope_fit .* t([imin:imax]))).^2)
40             ./ max(size(lnC([imin:imax])));
41
42 % 3D Model:
43 if dim == 3

```

```

44  % try to find the first root:
45  for beta=0.75.*pi:tolerance:pi
46      L = 1 - beta .* cot(beta);
47      intercept = log(2 .* L ./ (beta.^2 + (L .* (L - 1))));
48      if(abs(intercept - intercept_fit) <= sqrt(tolerance))
49          break;
50      end
51  end
52  % 1D Model:
53  elseif dim == 1
54      % try to find the first root:
55      for beta=0:tolerance:pi
56          L = beta .* tan(beta);
57          intercept = log(2 .* L ./ (beta.^2 + (L .* (L + 1))));
58          if(abs(intercept - intercept_fit) <= sqrt(tolerance))
59              break;
60          end
61      end
62  end
63
64  y = intercept_fit + slope_fit .* t;
65  y2 = intercept + slope_fit .* t;
66
67  % do plots if gfx == 1:
68  [...]
69
70  % results:
71  Dr2 = -1 .* slope_fit ./ beta.^2;
72  % L = L;
73  % beta = beta;
74  ysmooth = C_smooth;
75  linfit = exp([slope_fit intercept]);
76  ylinfit = exp(y2);
77
78  end

```

B.2. SigmaPlot macros

Listing B.4: Parameter calculation for the ZLC full-time solution

```

1  f1=col(4,9,9)*exp(-col(4,1,1)*D*t)
2  f2=f1/(col(4,1,1)+col(4,10,10))
3  f3=col(4,9,9)*exp(-col(4,2,2)*D*t)
4  f4=f3/(col(4,2,2)+col(4,10,10))
5  f5=col(4,9,9)*exp(-col(4,3,3)*D*t)
6  f6=f5/(col(4,3,3)+col(4,10,10))
7  f7=col(4,9,9)*exp(-col(4,4,4)*D*t)
8  f8=f7/(col(4,4,4)+col(4,10,10))
9  f9=col(4,9,9)*exp(-col(4,5,5)*D*t)
10 f10=f9/(col(4,5,5)+col(4,10,10))
11 f11=col(4,9,9)*exp(-col(4,6,6)*D*t)
12 f12=f11/(col(4,6,6)+col(4,10,10))
13 f13=col(4,9,9)*exp(-col(4,7,7)*D*t)

```

REFERENCES

```
14 f14=f13/(col(4,7,7)+col(4,10,10))
15 f15=col(4,9,9)*exp(-col(4,8,8)*D*t)
16 f16=f15/(col(4,8,8)+col(4,10,10))
17 f=f2+f4+f6+f8+f10+f12+f14+f16
18 fit f to y
19
20 [initial parameters]
21 D = 0.005
22
23 [constraints]
24 D > 0
25
26 [variables]
27
28 t=col(1)
29 y=col(2)
30
31 [option]
32 iterations = 100
33 tolerance = 0.0000001
```


Bibliography

- [1] K. S. W. Sing, D. H. Everett, R. A. W. Haul, L. Moscou, R. A. Pierotti, J. Rouquerol, and T. Siemieniewska. Reporting Physisorption Data for Gas Solid Systems with Special Reference to the Determination of Surface-Area and Porosity (Recommendations 1984). *Pure and Applied Chemistry*, 57(4):603–619, 1985.
- [2] C. G. Sonwane and Q. Li. Molecular simulation of RMM: Ordered mesoporous SBA-15 type material having microporous ZSM-5 walls. *Journal of Physical Chemistry B*, 109(38):17993–17997, 2005.
- [3] M. Kruk, M. Jaroniec, R. Ryoo, and S. H. Joo. Characterization of ordered mesoporous carbons synthesized using MCM-48 silicas as templates. *Journal of Physical Chemistry B*, 104(33):7960–7968, 2000.
- [4] M. Kruk, M. Jaroniec, T. W. Kim, and R. Ryoo. Synthesis and characterization of hexagonally ordered carbon nanotubes. *Chemistry of Materials*, 15(14):2815–2823, 2003.
- [5] H. J. Shin, R. Ryoo, M. Kruk, and M. Jaroniec. Modification of SBA-15 pore connectivity by high-temperature calcination investigated by carbon inverse replication. *Chemical Communications*, (4):349–350, 2001.
- [6] A. H. Lu, W. Schmidt, A. Taguchi, B. Spliethoff, B. Tesche, and F. Schuth. Taking nanocasting one step further: Replicating CMK-3 as a silica material. *Angewandte Chemie-International Edition*, 41(18):3489–+, 2002.
- [7] A. H. Lu, A. Kiefer, W. Schmidt, and F. Schuth. Synthesis of polyacrylonitrile-based ordered mesoporous carbon with tunable pore structures. *Chemistry of Materials*, 16(1):100–103, 2004.
- [8] A. Vinu, M. Miyahara, V. Sivamurugan, T. Mori, and K. Ariga. Large pore cage type mesoporous carbon, carbon nanocage: a superior adsorbent for biomaterials. *Journal of Materials Chemistry*, 15(48):5122–5127, 2005.
- [9] B. Sakintuna and Y. Yurum. Templated porous carbons: A review article. *Industrial and Engineering Chemistry Research*, 44(9):2893–2902, 2005.
- [10] R. K. Iler. The Chemistry of Silica: Solubility, Polymerization, Colloid and Surface Properties and Biochemistry. New York, 1979.
- [11] C. J. Brinker. Structure of sol-gel-derived glasses. *Glass Science and Technology*, 4A:169–230, 1990.

REFERENCES

- [12] C. J. Brinker, W. D. Drotning, and G. W. Scherer. A comparison between the densification kinetics of colloidal and polymeric silica gels. In *Better Ceramics Through Chemistry*, volume 32, New York, 1984. Materials Research Society.
- [13] J. S. Beck, J. C. Vartuli, W. J. Roth, M. E. Leonowicz, C. T. Kresge, K. D. Schmitt, C. T. W. Chu, D. H. Olson, E. W. Sheppard, S. B. McCullen, J. B. Higgins, and J. L. Schlenker. A New Family of Mesoporous Molecular-Sieves Prepared with Liquid-Crystal Templates. *Journal of the American Chemical Society*, 114(27): 10834–10843, 1992.
- [14] C. T. Kresge, M. E. Leonowicz, W. J. Roth, J. C. Vartuli, and J. S. Beck. Ordered Mesoporous Molecular-Sieves Synthesized by a Liquid-Crystal Template Mechanism. *Nature*, 359(6397):710–712, 1992.
- [15] J.M. Seddon and R.H. Templer. Polymorphism of Lipid-Water Systems. In R. Lipowsky and E. Sackmann, editors, *Handbook of Biological Physics*, pages 97–160. Elsevier Science B.V., 1995.
- [16] P. Behrens, A. Glaue, C. Haggenmuller, and G. Schechner. Structure-directed materials syntheses: Synthesis field diagrams for the preparation of mesostructured silicas. *Solid State Ionics*, 101:255–260, 1997.
- [17] C. A. Fyfe and G. Y. Fu. Structure Organization of Silicate Polyanions with Surfactants - a New Approach to the Syntheses, Structure Transformations, and Formation Mechanisms of Mesostructural Materials. *Journal of the American Chemical Society*, 117(38):9709–9714, 1995.
- [18] Q. S. Huo, D. I. Margolese, U. Ciesla, P. Y. Feng, T. E. Gier, P. Sieger, R. Leon, P. M. Petroff, F. Schuth, and G. D. Stucky. Generalized Synthesis of Periodic Surfactant Inorganic Composite-Materials. *Nature*, 368(6469):317–321, 1994.
- [19] Q. S. Huo, R. Leon, P. M. Petroff, and G. D. Stucky. Mesostructure Design with Gemini Surfactants - Supercage Formation in a 3-Dimensional Hexagonal Array. *Science*, 268(5215):1324–1327, 1995.
- [20] Q. S. Huo, D. I. Margolese, and G. D. Stucky. Surfactant control of phases in the synthesis of mesoporous silica-based materials. *Chemistry of Materials*, 8(5): 1147–1160, 1996.
- [21] T. W. Kim, F. Kleitz, B. Paul, and R. Ryoo. MCM-48-like large mesoporous silicas with tailored pore structure: Facile synthesis domain in a ternary triblock copolymer-butanol-water system. *Journal of the American Chemical Society*, 127(20):7601–7610, 2005.
- [22] F. Kleitz, T. W. Kim, and R. Ryoo. Phase domain of the cubic $im\bar{3}m$ mesoporous silica in the EO106PO70EO106-butanol-H₂O system. *Langmuir*, 22(1):440–445, 2006.

REFERENCES

- [23] F. Kleitz, L. A. Solvyov, G. M. Anilkumar, S. H. Choi, and R. Ryoo. Transformation of highly ordered large pore silica mesophases (Fm3m, Im3m and p6mm) in a ternary triblock copolymer-butanol-water system. *Chemical Communications*, (13): 1536–1537, 2004.
- [24] F. Kleitz, T. W. Kim, and R. Ryoo. Design of mesoporous silica at low acid concentrations in triblock copolymer-butanol-water systems. *Bulletin of the Korean Chemical Society*, 26(11):1653–1668, 2005.
- [25] V. T. Hoang, Q. L. Huang, M. Eic, T. O. Do, and S. Kaliaguine. Structure and diffusion characterization of SBA-15 materials. *Langmuir*, 21(5):2051–2057, 2005.
- [26] A. V. Neimark, P. I. Ravikovitch, M. Grun, F. Schuth, and K. K. Unger. Pore size analysis of MCM-41 type adsorbents by means of nitrogen and argon adsorption. *Journal of Colloid and Interface Science*, 207(1):159–169, 1998.
- [27] U. Ciesla and F. Schuth. Ordered mesoporous materials. *Microporous and Mesoporous Materials*, 27(2-3):131–149, 1999.
- [28] A. Sayari. Catalysis by crystalline mesoporous molecular sieves. *Chemistry of Materials*, 8(8):1840–1852, 1996.
- [29] X. S. Zhao, G. Q. M. Lu, and G. J. Millar. Advances in mesoporous molecular sieve MCM-41. *Industrial and Engineering Chemistry Research*, 35(7):2075–2090, 1996.
- [30] M. Jaroniec, M. Kruk, and A. Sayari. Adsorption methods for characterization of surface and structural properties of mesoporous molecular sieves. In *Mesoporous Molecular Sieves 1998*, volume 117 of *Studies in Surface Science and Catalysis*, pages 325–332. Elsevier Science Publ B V, Amsterdam, 1998.
- [31] M. Jaroniec, M. Kruk, and J. P. Olivier. Standard nitrogen adsorption data for characterization of nanoporous silicas. *Langmuir*, 15(16):5410–5413, 1999.
- [32] M. Jaroniec, J. Choma, and M. Kruk. On the applicability of the Horwath-Kawazoe method for pore size analysis of MCM-41 and related mesoporous materials. In *Characterization of Porous Solids V*, volume 128 of *Studies in Surface Science and Catalysis*, pages 225–234. Elsevier Science Bv, Amsterdam, 2000.
- [33] M. Kruk and M. Jaroniec. Gas adsorption characterization of ordered organic-inorganic nanocomposite materials. *Chemistry of Materials*, 13(10):3169–3183, 2001.
- [34] M. Kruk, V. Antochshuk, M. Jaroniec, and A. Sayari. New approach to evaluate pore size distributions and surface areas for hydrophobic mesoporous solids. *Journal of Physical Chemistry B*, 103(48):10670–10678, 1999.
- [35] W. W. Lukens, P. Schmidt-Winkel, D. Y. Zhao, J. L. Feng, and G. D. Stucky. Evaluating pore sizes in mesoporous materials: A simplified standard adsorption method and a simplified Broekhoff-de Boer method. *Langmuir*, 15(16):5403–5409, 1999.

REFERENCES

- [36] A. V. Neimark and P. I. Ravikovitch. Density functional theory of adsorption hysteresis and nanopore characterization. In *Characterization of Porous Solids V*, volume 128 of *Studies in Surface Science and Catalysis*, pages 51–60. Elsevier Science Bv, Amsterdam, 2000.
- [37] P. I. Ravikovitch, D. Wei, W. T. Chueh, G. L. Haller, and A. V. Neimark. Evaluation of pore structure parameters of MCM-41 catalyst supports and catalysts by means of nitrogen and argon adsorption. *Journal of Physical Chemistry B*, 101(19):3671–3679, 1997.
- [38] P. I. Ravikovitch, G. L. Haller, and A. V. Neimark. Density functional theory model for calculating pore size distributions: pore structure of nanoporous catalysts. *Advances in Colloid and Interface Science*, 77:203–226, 1998.
- [39] A. Sayari, P. Liu, M. Kruk, and M. Jaroniec. Characterization of large-pore MCM-41 molecular sieves obtained via hydrothermal restructuring. *Chemistry of Materials*, 9(11):2499–2506, 1997.
- [40] M. H. Lim and A. Stein. Comparative studies of grafting and direct syntheses of inorganic-organic hybrid mesoporous materials. *Chemistry of Materials*, 11(11):3285–3295, 1999.
- [41] T. Maschmeyer, F. Rey, G. Sankar, and J. M. Thomas. Heterogeneous Catalysts Obtained by Grafting Metallocene Complexes onto Mesoporous Silica. *Nature*, 378(6553):159–162, 1995.
- [42] K. Moller and T. Bein. Inclusion chemistry in periodic mesoporous hosts. *Chemistry of Materials*, 10(10):2950–2963, 1998.
- [43] P. Wu, T. Tatsumi, T. Komatsu, and T. Yashima. Postsynthesis, characterization, and catalytic properties in alkene epoxidation of hydrothermally stable mesoporous Ti-SBA-15. *Chemistry of Materials*, 14(4):1657–1664, 2002.
- [44] J. M. Kim, J. H. Kwak, S. Jun, and R. Ryoo. Ion-Exchange and Thermal-Stability of MCM-41. *Journal of Physical Chemistry*, 99(45):16742–16747, 1995.
- [45] R. Ryoo and S. Jun. Improvement of hydrothermal stability of MCM-41 using salt effects during the crystallization process. *Journal of Physical Chemistry B*, 101(3):317–320, 1997.
- [46] D. Y. Zhao, J. L. Feng, Q. S. Huo, N. Melosh, G. H. Fredrickson, B. F. Chmelka, and G. D. Stucky. Triblock copolymer syntheses of mesoporous silica with periodic 50 to 300 angstrom pores. *Science*, 279(5350):548–552, 1998.
- [47] D. Y. Zhao, Q. S. Huo, J. L. Feng, B. F. Chmelka, and G. D. Stucky. Non-ionic triblock and star diblock copolymer and oligomeric surfactant syntheses of highly ordered, hydrothermally stable, mesoporous silica structures. *Journal of the American Chemical Society*, 120(24):6024–6036, 1998.

REFERENCES

- [48] P. Alexandridis and T. A. Hatton. Poly(ethylene oxide)-poly(propylene oxide)-poly(ethylene oxide) block copolymer surfactants in aqueous solutions and at interfaces: thermodynamics, structure, dynamics, and modeling. *Colloids and Surfaces A: Physicochem. Eng. Aspects*, 96:1–46, 1995.
- [49] Y. Han, S. Wu, Y. Y. Sun, D. S. Li, F. S. Xiao, J. Liu, and X. Z. Zhang. Hydrothermally stable ordered hexagonal mesoporous aluminosilicates assembled from a triblock copolymer and preformed aluminosilicate precursors in strongly acidic media. *Chemistry of Materials*, 14(3):1144–1148, 2002.
- [50] Y. Sakamoto, M. Kaneda, O. Terasaki, D. Y. Zhao, J. M. Kim, G. Stucky, H. J. Shim, and R. Ryoo. Direct imaging of the pores and cages of three-dimensional mesoporous materials. *Nature*, 408(6811):449–453, 2000.
- [51] Ken Brakke. Surface Evolver, 2005.
- [52] P. I. Ravikovitch and A. V. Neimark. Density functional theory of adsorption in spherical cavities and pore size characterization of templated nanoporous silicas with cubic and three-dimensional hexagonal structures. *Langmuir*, 18(5):1550–1560, 2002.
- [53] P. I. Ravikovitch and A. V. Neimark. Experimental confirmation of different mechanisms of evaporation from ink-bottle type pores: Equilibrium, pore blocking, and cavitation. *Langmuir*, 18(25):9830–9837, 2002.
- [54] T. W. Kim, R. Ryoo, M. Kruk, K. P. Gierszal, M. Jaroniec, S. Kamiya, and O. Terasaki. Tailoring the pore structure of SBA-16 silica molecular sieve through the use of copolymer blends and control of synthesis temperature and time. *Journal of Physical Chemistry B*, 108(31):11480–11489, 2004.
- [55] K. Schumacher, P. I. Ravikovitch, A. Du Chesne, A. V. Neimark, and K. K. Unger. Characterization of MCM-48 materials. *Langmuir*, 16(10):4648–4654, 2000.
- [56] P. Y. Feng, X. H. Bu, and D. J. Pine. Control of pore sizes in mesoporous silica templated by liquid crystals in block copolymer-cosurfactant-water systems. *Langmuir*, 16(12):5304–5310, 2000.
- [57] D. Y. Zhao, J. Y. Sun, Q. Z. Li, and G. D. Stucky. Morphological control of highly ordered mesoporous silica SBA-15. *Chemistry of Materials*, 12(2):275–+, 2000.
- [58] R. Ryoo, C. H. Ko, M. Kruk, V. Antochshuk, and M. Jaroniec. Block-copolymer-templated ordered mesoporous silica: Array of uniform mesopores or mesopore-micropore network? *Journal of Physical Chemistry B*, 104(48):11465–11471, 2000.
- [59] A. Galarneau, H. Cambon, F. Di Renzo, and F. Fajula. True microporosity and surface area of mesoporous SBA-15 silicas as a function of synthesis temperature. *Langmuir*, 17(26):8328–8335, 2001.

REFERENCES

- [60] A. Galarneau, N. Cambon, F. Di Renzo, R. Ryoo, M. Choi, and F. Fajula. Microporosity and connections between pores in SBA-15 mesostructured silicas as a function of the temperature of synthesis. *New Journal of Chemistry*, 27(1):73–79, 2003.
- [61] S. Ruthstein, V. Frydman, and D. Goldfarb. Study of the Initial Formation Stages of the Mesoporous Material SBA-15 Using Spin-Labeled Block Co-polymer Templates. *Journal of Physical Chemistry B*, 108(26):9016–9022, 2004.
- [62] D. Brunel, N. Bellocq, P. Sutra, A. Cauvel, M. Lasperas, P. Moreau, F. Di Renzo, A. Galarneau, and F. Fajula. Transition-metal ligands bound onto the micelle-templated silica surface. *Coordination Chemistry Reviews*, 180:1085–1108, 1998.
- [63] F. Rouquerol, J. Rouquerol, and K. Sing. *Adsorption by powders and porous solids*. Acad. Press, 1999, 1999.
- [64] C. Sangwichien, G. L. Aranovich, and M. D. Donohue. Density functional theory predictions of adsorption isotherms with hysteresis loops. *Colloids and Surfaces a-Physicochemical and Engineering Aspects*, 206(1-3):313–320, 2002.
- [65] M. M. Dubinin, E. D. Zaverina, and L. V. Radushkevich. Sorbtsiya I Struktura Aktivnykh Ugley .1. Issledovanie Adsorbtsii Organicheskikh Parov. *Zhurnal Fizicheskoi Khimii*, 21(11):1351–1362, 1947.
- [66] M. M. Dubinin, A. V. Neimark, and V. V. Serpinskii. Modification of the Theory of a 3-Dimensional Filling of Micropores. *Bulletin of the Russian Academy of Sciences-Division of Chemical Science*, 41(1):5–9, 1992.
- [67] P. I. Ravikovitch, S. C. Odomhnaill, A. V. Neimark, F. Schuth, and K. K. Unger. Capillary hysteresis in nanopores: Theoretical and experimental studies of nitrogen adsorption on MCM-41. *Langmuir*, 11(12):4765–4772, 1995.
- [68] J. H. Deboer, B. C. Lippens, B. G. Linsen, Broekhof.Jc, Vandenhe.A, and T. J. Osinga. T-Curve of Multimolecular N₂-Adsorption. *Journal of Colloid and Interface Science*, 21(4):405–&, 1966.
- [69] J. H. Deboer, B. G. Linsen, Broekhof.Jc, and T. J. Osinga. Studies on Pore Systems in Catalysts .15. Influence of Geometrical Factor on T Curve Measured on Aerosil. *Journal of Catalysis*, 11(1):46–&, 1968.
- [70] M. Kruk, M. Jaroniec, and A. Sayari. Application of large pore MCM-41 molecular sieves to improve pore size analysis using nitrogen adsorption measurements. *Langmuir*, 13(23):6267–6273, 1997.
- [71] E.P. Barrett, L.G. Joyner, and P.P. Halenda. The Determination of Pore Volume and Area Distributions in Porous Substances. I. Computations from Nitrogen Isotherms. *Journal of the American Chemical Society*, 73:373–380, 1951.
- [72] Danny Schuring. *Diffusion in Zeolites: Towards a Microscopic Understanding*. PhD thesis, University Eindhoven, 2002.

REFERENCES

- [73] M. Jiang and M. Eic. Transport Properties of Ethane, Butane and Their Binary Mixtures in MFI-Type Zeolite and Zeolite-Membrane Systems. *Adsorption*, 9: 225–234, 2003.
- [74] S. Brandani, J. Hufton, and D. Ruthven. Self-Diffusion of Propane and Propylene in 5a and 13x Zeolite Crystals Studied by the Tracer Zlc Method. *Zeolites*, 15(7): 624–631, 1995.
- [75] S. Brandani and D. M. Ruthven. Analysis of ZLC desorption curves for gaseous systems. *Adsorption-Journal of the International Adsorption Society*, 2(2):133–143, 1996.
- [76] S. Brandani, M. Jama, and D. M. Ruthven. Counterdiffusion of p-xylene/benzene and p-xylene/o-xylene in silicalite studied by the zero-length column technique. *Industrial and Engineering Chemistry Research*, 39(3):821–828, 2000.
- [77] S. Brandani, M. A. Jama, and D. M. Ruthven. ZLC Measurements under non-linear conditions. *Chemical Engineering Science*, 55(7):1205–1212, 2000.
- [78] C. L. Cavalcante and D. M. Ruthven. Adsorption of Branched and Cyclic Paraffins in Silicalite .1. Equilibrium. *Industrial and Engineering Chemistry Research*, 34(1): 177–184, 1995.
- [79] C. L. Cavalcante and D. M. Ruthven. Adsorption of Branched and Cyclic Paraffins in Silicalite .2. Kinetics. *Industrial and Engineering Chemistry Research*, 34(1): 185–191, 1995.
- [80] W. L. Duncan and K. P. Möller. A 'zero length' criterion for ZLC chromatography. *Chemical Engineering Science*, 55:5415–5420, 2000.
- [81] S. Brandani and D. M. Ruthven. Analysis of Zlc Desorption Curves for Liquid-Systems. *Chemical Engineering Science*, 50(13):2055–2059, 1995.
- [82] D. M. Ruthven and P. Stapleton. Measurement of Liquid-Phase Counter-Diffusion in Zeolite Crystals by the Zlc Method. *Chemical Engineering Science*, 48(1):89–98, 1993.
- [83] W. L. Duncan and K. P. Möller. The effect of a crystall siye distribution on ZLC experiments. *Chemical Engineering Science*, 57:2641 – 2652, 2002.
- [84] S. Brandani and D. M. Ruthven. Moments analysis of the zero length column method. *Industrial and Engineering Chemistry Research*, 35(1):315–319, 1996.
- [85] S. Brandani, C. Cavalcante, A. Guimaraes, and D. Ruthven. Heat effects in ZLC experiments. *Adsorption-Journal of the International Adsorption Society*, 4(3-4): 275–285, 1998.
- [86] C. L. Cavalcante, S. Brandani, and D. M. Ruthven. Evaluation of the main diffusion path in zeolites from ZLC desorption curves. *Zeolites*, 18(4):282–285, 1997.

REFERENCES

- [87] D. Ruthven and F. Brandani. ZLC response for systems with surface resistance control. *Adsorption-Journal of the International Adsorption Society*, 11(1):31–34, 2005.
- [88] H. Vinh-Thang, Q. L. Huang, M. Eic, D. Trong-On, and S. Kaliaguine. Adsorption of C-7 hydrocarbons on biporous SBA-15 mesoporous silica. *Langmuir*, 21(11): 5094–5101, 2005.
- [89] F. Kleitz, S. H. Choi, and R. Ryoo. Cubic Ia3d large mesoporous silica: synthesis and replication to platinum nanowires, carbon nanorods and carbon nanotubes. *Chemical Communications*, (17):2136–2137, 2003.
- [90] K. Miyazawa and S. Inagaki. Control of the microporosity within the pore walls of ordered mesoporous silica SBA-15. *Chemical Communications*, (21):2121–2122, 2000.
- [91] P. I. Ravikovitch and A. V. Neimark. Characterization of micro- and mesoporosity in SBA-15 materials from adsorption data by the NLDT method. *Journal of Physical Chemistry B*, 105(29):6817–6823, 2001.
- [92] T. W. Kim, R. Ryoo, K. P. Gierszal, M. Jaroniec, L. A. Solovyov, Y. Sakamoto, and O. Terasaki. Characterization of mesoporous carbons synthesized with SBA-16 silica template. *Journal of Materials Chemistry*, 15(15):1560–1571, 2005.
- [93] M. Eic and D. M. Ruthven. A New Experimental-Technique for Measurement of Intracrystalline Diffusivity. *Zeolites*, 8(1):40–45, 1988.
- [94] F. Brandani, D. Ruthven, and C. G. Coe. Measurement of adsorption equilibrium by the zero length column (ZLC) technique part 1: Single-component systems. *Industrial and Engineering Chemistry Research*, 42(7):1451–1461, 2003.
- [95] V. R. Choudhary, V. S. Nayak, and T. V. Choudhary. Single-Component Sorption/Diffusion of Cyclic Compounds from Their Bulk Liquid Phase in H-ZSM-5 Zeolite. *Industrial and Engineering Chemistry Research*, 36:1812 – 1818, 1997.
- [96] M. Schunack, T. R. Linderoth, F. Rosei, E. Laegsgaard, I. Stensgaard, and F. Besenbacher. Long Jumps in the Surface Diffusion of Large Molecules. *Physical Review Letters*, 88(15), 2002.
- [97] S. C. Wang, J.D. Wrigley, and G. Ehrlich. Atomic jump lengths in surface diffusion: Re, Mo, Ir and Rh on W(211). *Journal of Chemical Physics*, 91(8):5087 – 5096, 1989.
- [98] V. T. Hoang, Q. L. Huang, M. Eic, T. O. Do, and S. Kaliaguine. Effect of the Intrawall Microporosity on the Diffusion Characterization of Biporous SBA-15 Materials. *Studies in Surface Science and Catalysis*, in press, 2005.
- [99] J. M. Esparza, M. L. Ojeda, A. Campero, G. Hernandez, C. Felipe, M. Asomoza, S. Cordero, I. Kornhauser, and F. Rojas. Development and sorption characterization of some model mesoporous and microporous silica adsorbents. *Journal of Molecular Catalysis a-Chemical*, 228(1-2):97–110, 2005.

REFERENCES

- [100] L. J. Gurvitsch. *Russian Journal of Physical Chemistry*, 47:805, 1915.
- [101] E. van Bavel, V. Meynen, P. Cool, K. Lebeau, and E. F. Vansant. Adsorption of Hydrocarbons on Mesoporous SBA-15 and PHTS Materials. *Langmuir*, 21: 2447–2453., 2005.
- [102] Y. Sun, Y. Han, L. Yuan, S. Ma, D. Jiang, and F.-S. Xiao. Microporosity in Ordered Mesoporous Aluminosilicates Characterized by Catalytic Probing Reactions. *Journal of Physical Chemistry B*, 107(8):1853–1857, 2003.
- [103] B. L. Newalkar, N. V. Choudary, P. Kumar, S. Komarneni, and T. S. G. Bhat. Exploring the potential of mesoporous silica, SBA-15, as an adsorbent for light hydrocarbon separation. *Chemistry of Materials*, 14(1):304–309, 2002.
- [104] C. Seebacher, C. Hellriegel, F.-W. Deeg, C. Brauchle, S. Altmaier, P. Behrens, and K. Mullen. Observation of Translational Diffusion of Single Terrylenediimide Molecules in a Mesostructured Molecular Sieve. *Journal of Physical Chemistry B*, 106(22):5591–5595, 2002.